

# Multi-model analysis of the impact of water vapor on the radiative impacts forcing of volcanic aerosols after the 2022 Hunga eruption indicates a significant cooling contribution from the volcanic plume Eruption

Ilaria Quaglia<sup>1</sup>, Daniele Visioni<sup>1,2</sup>, Ewa M. Bednarz<sup>3,4</sup>, Yunqian Zhu<sup>3,4</sup>, Georgiy Stenchikov<sup>5</sup>, Valentina Aquila<sup>6</sup>, Cheng-Cheng Liu<sup>7</sup>, Graham W. Mann<sup>8</sup>, Yifeng Peng<sup>9</sup>, Takashi Sekiya<sup>10</sup>, Simone Tilmes<sup>1</sup>, Xinyue Wang<sup>11</sup>, Shingo Watanabe<sup>12</sup>, Pengfei Yu<sup>13</sup>, Jun Zhang<sup>1</sup>, Wandu Yu<sup>14</sup>, and Zhihong Zhuo<sup>15</sup>

<sup>1</sup>NSF National Center for Atmospheric Research, Boulder, CO, USA

<sup>2</sup>Department of Earth and Atmospheric Sciences, Cornell University, USA

<sup>3</sup>Cooperative Institute for Research in Environmental Sciences (CIRES), University of Colorado, Boulder, USA

<sup>4</sup>NOAA Chemical Sciences Laboratory, Boulder, USA

<sup>5</sup>Physical Science and Engineering Division, King Abdullah University of Science and Technology, Jeddah, Saudi Arabia

<sup>6</sup>American University, Department of Environmental Science, Washington, DC, USA

<sup>7</sup>Laboratory for Atmospheric and Space Physics, University of Colorado Boulder, Boulder, CO, USA

<sup>8</sup>School of Earth and Environment, University of Leeds, Leeds, UK

<sup>9</sup>Lanzhou University, Lanzhou, China

<sup>10</sup>Japan Agency for Marine-Earth Science and Technology (JAMSTEC), Yokohama, Japan

<sup>11</sup>Department of Atmospheric and Oceanic Sciences, University of Colorado Boulder, Boulder, USA

<sup>12</sup>Advanced Institute for Marine-Ecosystem Change, Tohoku University, Sendai, Japan

<sup>13</sup>Jinan University, Guangzhou, China

<sup>14</sup>Lawrence Livermore National Laboratory, USA

<sup>15</sup>Department of Earth and Atmospheric Sciences, University of Quebec in Montreal, Montreal (Quebec), Canada

**Correspondence:** Ilaria Quaglia (iquaglia@ucar.edu)

**Abstract.** On January 15, 2022, the Hunga volcano eruption released unprecedented amounts of water vapor into the atmosphere alongside a modest amount of SO<sub>2</sub>. In this work we analyse results from multiple Earth system models as part of the Hunga Tonga-Hunga Ha'apai Volcano Impact Model Observation Comparison Project.

Our results show a good model agreement over the climatic outcomes of the eruption, overall indicating a significant negative radiative forcing from the Hunga eruption. The multi-model mean of global instantaneous radiative forcing averaged over 2022-2023 is estimated at  $-0.19 \pm 0.04 \text{ W/m}^2$   $-0.06 \text{ W m}^{-2}$  at the top-of-atmosphere (TOA), and  $-0.16 \pm 0.03 \text{ W/m}^2$   $-0.06 \text{ W m}^{-2}$  at the surface. Simulations with free-running meteorology and climatological sea surface temperatures and sea ice yield a global mean TOA forcing of  $-0.14 \pm 0.10 \text{ W/m}^2$   $\text{m}^{-2}$  across two models for the first 2 years, decreasing to  $-0.09 \pm 0.10 \text{ W/m}^2$   $\text{m}^{-2}$  on average between 2022 and 2027. However, these global values may be underestimated by about 50%, considering that recent SO<sub>2</sub> injection retrievals suggest nearly twice the amount than the 0.5 Tg-SO<sub>2</sub> used in the protocol. We also find that the contribution from added stratospheric water vapor is minimal and that the injected SO<sub>2</sub> and the resulting formation of stratospheric sulfate dominate the radiative forcing. However, water vapor played a key role in the initial aerosol growth,

leading to a stronger negative radiative forcing during the first six months after the eruption compared to simulations without water vapor co-injection.

## 15 1 Introduction

Explosive volcanic eruptions that release large amounts of SO<sub>2</sub> into the stratosphere have long been identified as a significant contributor to the global energy budget (Schmidt et al., 2018). The release of SO<sub>2</sub> into the stratosphere results in the formation of sub-micron, supercooled sulfate aerosols which efficiently reflect incoming solar radiation, resulting in a negative forcing at the top of the atmosphere and thus a corresponding surface cooling (Kremser et al., 2016). While of-  
20 ten studies of volcanic aerosols' impact on climate focus on very large eruptions like Mt. Pinatubo, that erupted in 1991 (Quaglia et al., 2023) releasing anywhere between 10 and 20 Tg-SO<sub>2</sub> in a few days (Baran and Foot, 1994; Fisher et al., 2019), ~~the most~~ recent decades have ~~seldom-seen~~ seen fewer eruptions with injections ~~larger than~~ exceeding a few Tg of SO<sub>2</sub> (~~Carn et al., 2017; Schmidt et al., 2018; Brodowsky et al., 2021~~). ~~While smaller than Pinatubo, even one "moderate" eruption~~ ean (~~Carn et al., 2017; Brodowsky et al., 2021~~). However, moderate eruptions, such as Raikoke (2019), Ulawun (2019), Ambae,  
25 La Soufrière (2021), and Hunga Tonga (2022), have received increasing attention in recent research, offering valuable insights into aerosol microphysics, plume dynamics, and radiative forcing at the top of the atmosphere (Kloss et al., 2021; Wrana et al., 2023). Despite their smaller scale compared to Pinatubo, moderate eruptions can still substantially double the quiescent stratospheric sulfate burden (~~Brodowsky et al., 2024~~), ~~and their analyses can provide very important insights into aerosol microphysics, plume evolution and associated top-of-atmosphere radiative forcing (Brodowsky et al., 2021; Li et al., 2023)~~ (Schmidt et al., 2018; Andersson et al., 2023), underscoring the importance of including these events in both climate modeling and aerosol research.  
30

The co-emission of other byproducts of volcanism, together with sulfate, is not infrequent: some ash and water vapor usually reaches the stratosphere (Zhu et al., 2020), and in some occasions chlorine and bromine in significant quantities are also co-injected, but whether they reach the stratosphere are debatable (Staunton-Sykes et al., 2021). Hunga ~~Tonga-Hunga Ha'apai~~  
35 ~~(Hunga)~~ erupted on January 15 2022 in the South Pacific, releasing ~~unprecedented amounts~~ an amount of materials into the atmosphere unprecedented in the satellite era (Carr et al., 2022). Current estimates of injected material are  $146 \pm 5$  Tg of water vapor based on Aura Microwave Limb Sounder (MLS) retrievals (Millán et al., 2022), with a broader range for injected SO<sub>2</sub> ~~between~~, ranging from  $0.41 \pm 0.02$  Tg of SO<sub>2</sub> for MLS ~~and~~  $1.6 \pm 0.5$  to values greater than 1.0 Tg of SO<sub>2</sub> ~~for~~ from the Infrared Atmospheric Sounding Interferometer (IASI) (Sellitto et al., 2024). While the amount of injected sulfur was within the  
40 range of many ~~minor~~ moderate past explosive volcanic eruptions, the amount of water vapor co-injected was unprecedented in the historical record, representing roughly  $\sim 10\%$  of all background stratospheric water vapor. ~~The height of the injected SO<sub>2</sub> was also, by many standards, unprecedented, reaching a height of~~ Although comparable increases in moisture can be achieved through the indirect pathway, such as during Pinatubo-like eruptions in the tropics (Kroll and Schmidt, 2024), what makes Hunga eruption truly unprecedented aspect of this eruption was the height at which the overall volcanic plume was  
45 injected, reaching up to 55 km (Carr et al., 2022). Early estimates assumed the water vapor forcing would result in a small net

warming (Jenkins et al., 2023). However, other estimates found that the sulfate aerosols produced by the co-injections of SO<sub>2</sub>, which normally oxidize to form sulfuric-acid aerosols, would result in a significant negative forcing after the ~~plume-volcanic~~ cloud spread uniformly (Sellitto et al., 2022; Zhu et al., 2022; Schoeberl et al., 2024), larger than the water vapor forcing. Later modeling analyses by Stenchikov et al. (2025), using WRF-chem, also found a negative forcing by considering similar factors.

50 Notably, the ~~increased-size-of-aerosols-formed-under~~ conditions of significant stratospheric hydration (~~Zhu et al., 2022~~) has been suggested as an important factor contributing to the ~~significant-radiative-impact~~ substantial radiative impact of the Hunga cloud, even in the case of a modest SO<sub>2</sub> injection, as it promoted faster aerosol growth, allowing particles to reach sizes that are optically efficient scatterers (Zhu et al., 2022; Li et al., 2024; Sellitto et al., 2025).

55 As part of the Hunga Tonga-Hunga Ha'apai (HTHH) Impacts activity that was established in the World Climate Research Programme (WCRP) Atmosphere Processes And their Role in Climate (APARC), a multi-model-observation intercomparison named the Hunga Tonga-Hunga Ha'apai Volcano Impact Model Observation Comparison (HTHH-MOC) Project was proposed in Zhu et al. (2025) with the aim to better ascertain the radiative and climatic impacts of Hunga in a multi-model context and to try and separate the volcanic impacts from other natural or anthropic perturbations in the same years (Forster et al., 2023),  
60 especially in light of the "unprecedented" surface temperature warming in 2023 (Cattiaux et al., 2024; Quaglia and Visioni, 2024). Other parallel works within this same project discuss in depth changes to stratospheric water vapor, aerosols, temperature, and ozone (Zhuo et al., 2025) and potential impacts on climate (Bednarz et al., 2025). In this paper, we ~~focus on~~ examine the radiative forcing ~~arising-resulting~~ from these changes ~~by some of the~~ using a multi-model approach, by using several proposed HTHH-MOC experiments~~in a multi-model context, highlighting~~. Our goal is to highlight the sources of agree-  
65 ment ~~across models as well as differences in the estimated forcing magnitude~~ and differences across models in estimating the magnitude of the forcing. Three different atmospheric setups are considered for the Hunga eruption simulation: (1) temperature and meteorology nudged to observations; (2) a free running meteorology setup with fixed sea surface temperature and sea ice extent; (3) and free-running meteorology setup with interactive ocean. The framework allows to distinguish the contributions from the direct interactions between the forcing agent and radiation, the rapid adjustments to these forcings, and slower climate  
70 feedback. Additionally, sensitivity studies performed within the nudged setup compare the effects of SO<sub>2</sub>-only and water vapor-only injections with the combined impact of both. The long-term evolution of Hunga water vapor and aerosols in the free-running models provides broader projections of the eruption climate impact. This comprehensive approach differentiates our study from previous work by integrating multiple experimental setups to better capture the complex interactions and feedbacks associated with the eruption.

75

## 2 Methods

### 2.1 Models and simulations

We use a suite of experiments described in depth in Zhu et al. (2025), which includes also a detailed descriptions of the models under analyses. The first set of experiments is a 2-year experiment over 2022-2023 with nudged temperature and meteorology as well as observed sea surface temperatures (SSTs) and sea ice (Exp2a in Zhu et al. (2025), here denoted "Nudged"; note this is distinct from Exp2b, not included in this study, which does not require prognostic aerosols). The second set of experiments is a 10-year long experiment over 2022-2031 with free running meteorology, using either imposed climatological SSTs and sea ice (Exp1\_fixedSST in Zhu et al. (2025), here "Fixed-SST") or with the atmosphere model coupled with the ocean (Exp1\_coupled, here "Coupled"). Each ~~set of experiments consists of simulations with experiment includes at least one simulation that involves the combined injection of 0.5 Tg of SO<sub>2</sub> and 150 Tg of H<sub>2</sub>O injections ("SO<sub>2</sub>andH<sub>2</sub>O") as well as control simulations, alongside a control simulation without any injections ("NoVolc"). Some models also performed additional single forcing experiments with injection of "NoVolc").~~ The Nudged experiment also includes single-forcing simulations that inject only SO<sub>2</sub> ("SO<sub>2</sub>only") or only H<sub>2</sub>O ("H<sub>2</sub>Oonly"). The location, altitude, and amount injected are different between models in order to better match the observed plume in the first couple of days, but they remain consistent across experiments between models. ~~Detailed injection settings for each model are~~ Models account for the interactive coupling between aerosol, water vapor, radiation, and dynamics, allowing the fast descent due to water vapor longwave cooling (Sellitto et al., 2022) to be simulated through this coupling. A summary of the experiments is provided in Table 1, and detailed model-specific injection settings are listed in Table 2.

Nudged was conducted by 5 models: the Whole Atmosphere Community Climate Model version 6 (WACCM6; Gettelman et al., 2019; Davis et al., 2023) coupled with the four-mode modal aerosol module (MAM4, Liu et al., 2012, 2016; Mills et al., 2016) and the Community Aerosol and Radiation Model for Atmospheres (CARMA; Tilmes et al., 2023), WACCM6-MAM and WACCM6-CARMA, respectively; the Model for Interdisciplinary Research On Climate - CHemical Atmospheric general circulation model for Study of atmospheric Environment and Radiative forcing version 6 (MIROC-CHASER; Sekiya et al., 2016); the atmospheric component of CESM1, the Community Atmosphere Model version 5 (CAM5; Lamarque et al., 2012) using the sectional aerosol microphysics model CARMA (CAM5-CARMA; Yu et al., 2015), and the UK Earth System Model version 1.1 (UKESM; Mulcahy et al., 2023). Fixed-SST was carried out with two models, WACCM6-MAM and MIROC-CHASER, while only WACCM6-MAM participated in Coupled. WACCM6-MAM ran 30-member ensembles for both Fixed-SST and Coupled, whereas MIROC-CHASER ran 10-member ensembles for Fixed-SST. Further information about the participating models can be found in the references above, as well as in Zhu et al. (2025).

### 2.2 Observational datasets

We use two observational datasets in this study: the Global Space-based Stratospheric Aerosol Climatology version 2.22 (GloSSAC, NASA/LARC/SD/ASDC) for zonal monthly-mean stratospheric aerosol optical depth (AOD), and the Stratospheric Water and Ozone Satellite Homogenized dataset version 2.6 (SWOOSH, Davis et al., 2016) for water vapor.

**Table 1.** Summary of experiments

<u>Experiment name</u> <u>(former name in Zhu et al., 2025)</u>	<u>Meteorological configuration</u>	<u>Year simulated</u>	<u>Subset of experiment included</u>
<u>Nudged (Exp2a)</u>	<u>Nudged wind and temperature,</u> <u>fixed sea surface temperatures</u>	<u>2022-2023</u>	<u>NoVolc</u> <u>SO2andH2O</u> <u>SO2only</u> <u>H2Oonly</u>
<u>Fixed-SST (Exp1_fixedSST)</u>	<u>Free running meteorology,</u> <u>fixed sea surface temperatures</u>	<u>2022-2031</u>	<u>NoVolc</u> <u>SO2andH2O</u>
<u>Coupled (Exp1_coupled)</u>	<u>Free running meteorology,</u> <u>atmospheric-ocean coupling</u>	<u>2022-2031</u>	<u>NoVolc</u> <u>SO2andH2O</u>

**Table 2.** Injection parameters. Adapted from Table 7 in Zhu et al. (2025)

Model	H <sub>2</sub> O injected	H <sub>2</sub> O altitude	SO <sub>2</sub> injected	SO <sub>2</sub> altitude	Injection location
WACCM6-MAM	150 Tg	25-35 km	0.5 Tg	20-28 km	22-14°S, 182-186°E
WACCM6-CARMA	150 Tg	25-35 km	0.5 Tg	26.5-36 km	22-6°S, 182.5-202.5°E
MIROC-CHASER	150 Tg	25-30 km	0.5 Tg	25-30 km	22-14°S, 182-186°E
CAM5-CARMA	150 Tg	25-35 km	0.5 Tg	20-28 km	22-14°S, 182-186°E
UKESM	150 Tg	25-30 km	0.5 Tg	25-30 km	22-14°S, 182-186°E

110 GloSSAC provides a long-term and global record of stratospheric aerosol properties, including the stratospheric AOD at  
525 nm used here. It is primarily based on Stratospheric Aerosol Gas Experiment (SAGE) measurements up to mid-2005, with  
Optical Spectrograph and Infrared Imaging System and Cloud-Aerosol Lidar and Infrared Pathfinder Satellite Observations  
used thereafter, and SAGE III extending the climatology to the present. Additional data from other satellites, as well as  
ground-based, airborne, and balloon-borne instruments, are included to fill observational gaps (Thomason et al., 2018; Kovilakam et al., 20  
115 . Although SAGE III data have limited spatial and temporal coverage, particularly during the first weeks following the Hunga  
eruption, they are considered robust because they rely on solar occultation and do not require assumptions about aerosol type or  
particle size distribution. In contrast, limb-scatter datasets such as Ozone Mapping and Profiler Suite Limb Profiler (OMPS-LP),

used for comparison in Zhuo et al. (2025), depend on additional assumptions about aerosol properties (Kovilakam et al., 2025). For these reasons, GloSSAC is adopted as the primary observational reference, providing a consistent and reliable basis for evaluating modeled stratospheric aerosol evolution over longer timescales.

120 SWOOSH is a long-term and global record of stratospheric ozone and water vapor measurements from multiple satellite instruments (SAGE II, SAGE III, Halogen Occultation Experiment, Upper Atmosphere Research Satellite Microwave Limb Sounder, and Earth Observing System Aura Microwave Limb Sounder) spanning 1984 to the present.

### 2.3 Radiative forcing estimations

There are important differences ~~between estimates of radiative forcing among the radiative forcing estimates~~ of volcanic eruptions derived from nudged simulations ~~referred to as~~, which provide the instantaneous radiative forcing (IRF) ~~that from~~; Eq. 1); free-running atmosphere-only simulations ~~conventionally termed~~, which yield the effective radiative forcing (ERF; Eq. 2), following the definition ~~by Forster et al. (2016) and that form of Forster et al. (2016)~~; and fully coupled simulations with ~~interactive ocean referred to generally an interactive ocean, which are generally referred to~~ as radiative forcing (RF; Eq. 3).

130 IRF represents the combined effect of direct interactions between the forcing agent and radiation, as well as interactions between the forcing agent and clouds (Smith et al., 2018). ERF, defined by Myhre et al. (2013) as "change in the net TOA downward radiative flux after allowing for atmospheric temperatures, water vapour and clouds to adjust, but with surface temperature or a portion of surface conditions unchanged", is the sum of IRF and rapid adjustments. These rapid adjustments which occur over weeks to months, before global-mean surface temperatures can respond, are due to changes in tropospheric and stratospheric temperature, water vapor, surface albedo, and clouds, and are distinct from slower feedbacks that are driven by surface temperature changes (Smith et al., 2018; Sherwood et al., 2015). In coupled model simulations, RF includes ~~the instantaneous radiative forcing (IRF)~~ IRF, rapid adjustments to that forcing, and slower climate feedbacks resulting from the coupled ocean-atmosphere response (Chung and Soden, 2015).

140 IRF is calculated in climate models using a double radiation call that excludes aerosols from online radiative calculations ("Clean-Sky") following the method proposed in Stenchikov et al. (1998) in order to separate the contribution of aerosols from that of other components. Since nudging reduces variability in meteorological fields, it typically limits any stratospheric temperature adjustments, as radiative forcing is calculated as the difference between the perturbed and unperturbed case. As a result, the IRF from aerosols and water vapor, either combined or individually, can be approximated using the corresponding Nudged experiments ~~(Eq. (4) and (5), respectively)~~. In the case of WACCM6-MAM simulations, both methodologies have been applied. Notably, in contrast to previous studies, all forcing estimates presented here treat stratospheric water vapor as a forcing rather than a feedback, due to its direct injection.

In summary, the following sections explain how the different radiative forcing estimates are calculated. ~~The term  $F_{control}$  refers to background simulations without any injection, while  $F_{volc}$  is used to indicate simulations that include volcanic forcing.~~

Radiative forcing is calculated under both Clear-Sky (CS, without clouds) and All-Sky (AS, including the effects of clouds) conditions. Unless otherwise specified, all values are assumed to be calculated under Clear-Sky conditions.

$$RF = F_{volc}^{clear} - F_{control}^{clear}: \text{Clear-Sky forcing from Coupled, including both injections of water vapor and SO}_2.$$

$$IRF = F_{SO2andH2O,Nudged} - F_{NoVolc,Nudged} \quad (1)$$

$$155 \quad ERF = F_{SO2andH2O,Fixed-SST} - F_{NoVolc,Fixed-SST} \quad (2)$$

$$RF = F_{SO2andH2O,Coupled} - F_{NoVolc,Coupled} \quad (3)$$

$$IRF_{aerosol} = F_{SO2only,Nudged} - F_{NoVolc,Nudged} \quad (4)$$

$$IRF_{gas} = F_{H2Oonly,Nudged} - F_{NoVolc,Nudged} \quad (5)$$

$$ERF = F_{volc}^{clear} - F_{control}^{clear}: \text{Clear-Sky forcing from Fixed-SST, including both injections of water vapor and SO}_2.$$

$$160 \quad IRRF = F_{volc}^{clear} - F_{control}^{clear}: \text{Clear-Sky forcing from Nudged-SO}_2\text{andH}_2\text{O, including both injections of water vapor and SO}_2.$$

$$IRF_{aerosol} = F_{volc}^{clear} - F_{control}^{clear}: \text{Clear-Sky forcing from Nudged-SO}_2\text{only, including only injections of SO}_2.$$

$$IRF_{gas} = F_{volc}^{clear} - F_{control}^{clear}: \text{Clear-Sky forcing, including only injections of H}_2\text{O in Nudged-H}_2\text{Oonly.}$$

165  $F^{clean}$  refers to Clean-Sky calculations (excluding aerosols) and is available only in In WACCM6-MAM, where it is derived using a second estimate of IRF for aerosols (sulfate, black carbon, primary organic matter, secondary organic aerosols, sea salt, and dust) and gases (water vapor, dioxygen, carbon dioxide, ozone, nitrous, methane, chlorofluorocarbons) is derived through a double radiation call. In this configuration, a second estimate of the instantaneous radiative forcing from aerosols and gases separately, as calculated below: (Eq. (6) and (7), respectively). Within this approach,  $F^{clean}$  denotes the Clean-Sky calculation, which excludes aerosols.

$$170 \quad IRRF_{aerosol} = (F_{volc}^{clear} - F_{volc}^{clean,clear}) - (F_{control}^{clear} - F_{control}^{clean,clear})$$

$$IRF_{aerosol} = (F_{SO2andH2O,Nudged} - F_{NoVolc,Nudged}) - (F_{SO2andH2O,Nudged}^{clean} - F_{NoVolc,Nudged}^{clean}) \quad (6)$$

$$IRF_{gas} = F_{SO2andH2O,Nudged}^{clean} - F_{NoVolc,Nudged}^{clean} \quad (7)$$

$$IRRF_{gas} = F_{volc}^{clean,clear} - F_{control}^{clean,clear}$$

We calculate RF at three key atmospheric levels - top of the atmosphere (TOA), tropopause (TROP), and surface (SURF) - as the sign and magnitude of RF can differ by altitude and carry distinct physical implications. Radiative forcing at TOA reflects the overall perturbation to the Earth's energy budget and is commonly used to estimate the potential influence on global average temperature. At the tropopause, RF captures the net energy change affecting the coupled troposphere-surface system, and is considered less affected by upper stratospheric processes and better represents tropospheric heating. In contrast, RF at the surface does not directly correspond to surface temperature responses but is more relevant for understanding impacts on the hydrological cycle, particularly changes in precipitation patterns (Ramaswamy et al., 2018).

### 3 Results and discussion

We present first the results based on the nudged simulations (Section Sect. 3.1), as this experiment was done by more models (five) and the use of observed meteorological conditions also allows us to better distinguish the overall radiative impact by removing natural variability. Since the same nudging (of temperature and horizontal wind) was applied in both the control and the volcanic injection experiments, taking the difference between the two simulations, as done in Fig. 1, isolates the direct radiative forcing from the volcanic material, as any temperature response cancels out. Following that, we provide analyses of the two models which provided the 10-year long free-running simulations with prescribed climatological SSTs and sea ice (Sect. 3.2): these analyses allow us to understand the long-term behavior of the forcing as well as include the combined chemical and dynamical impacts and temperature adjustments. Finally, we complete those with an analyses of fully-coupled simulations in WACCM6-MAM (Sect. 3.3). In this case, we compare the results from the three different types of simulations within the same model, coupled with analyses of the double-radiation call described in the methods above, to discuss and quantify the different contribution to the forcings analyses elsewhere.

#### 3.1 Multi-model comparison of instantaneous radiative forcing in the nudged simulations

Figure 1 shows a timeseries of zonal mean TOA IRF under clear-sky conditions from the nudged simulations. IRF accounts for the IRF includes all optically active components, including such as stratospheric aerosols, water vapor, ozone, and polar stratospheric clouds (PSCs). For model intercomparison, we use clear-sky forcing to minimize uncertainties associated with aerosol-cloud interactions that arise from differences in cloud parameterizations among models.

All five models show qualitative agreement in the spatial distribution of the forcing, with the response IRF under clear-sky conditions at TOA (Fig. 1), at TROP (Fig. A1), and at SURF (Fig. A2). At each level, the response is primarily located in the Southern Hemisphere (SH). Therefore; therefore, most of the following analyses will focus on the SH only. The spatial-

A consistent pattern of negative forcing, initially peaking appears across models in both the SO<sub>2</sub> and H<sub>2</sub>O and SO<sub>2</sub> only experiments (first and second columns in Figs. 1, A1, A2). This forcing peaks in the tropics during the first few months and then moving to the mid-to-high southern following the eruption and then moves to mid- to high-southern latitudes by 2023, is consistent across models. Likewise, all models simulate a with substantial negative forcing persisting through the end of 2023; and show similar results in attributing forcing primarily to aerosols (second column in Fig. 1), with mostly negligible responses seen under only the H<sub>2</sub>O injection in the SH. Likewise, all models simulate a negligible IRF from the H<sub>2</sub>O only experiment (third column in Fig. 1) of the same figures). Therefore, the models consistently attribute nearly all of the radiative forcing to the aerosol perturbations rather than to the injected water vapor.

210

Global and hemispheric means are shown in Fig. 2 as show the multi-model averages, with one standard deviation indicating the average and inter-model spread. At the TOA, models generally show a weak and negative water vapor forcing (as diagnosed from the), and highlight the magnitude of the IRF in each injection experiment. These means further clarify that the IRF

from H2Oonly simulations). At the tropopause (second column in Fig. 2), the radiative forcing from water vapor is indeed negligible: it is slightly negative at TOA (first column) and slightly positive at TROP and SURF (second and third columns). This behavior results from the vertical distribution of water vapor in the stratosphere and the lack of stratospheric temperature adjustment, which together increase outgoing longwave radiation while enhancing downward longwave re-emission. Especially at the surface, the IRF remains positive but very small. Regarding, as the radiative forcing is dominated by sensible and latent heat fluxes, which are controlled by the prescribed surface temperature in these simulations.

For the aerosol forcing, which thus constitutes essentially the entirety of the Hunga forcing perturbation, models generally show good agreement over the time evolution of the forcing but with some radiative forcing, the models generally agree on its temporal evolution but exhibit substantial differences in its magnitude. The multi-model mean TOA IRF from SO2andH2O is  $-0.35 \pm 0.08 \text{ W/m}^2$  averaged  $0.12 \text{ W m}^{-2}$  over  $60^\circ\text{S}$  to  $0^\circ\text{S}$  for the period 2022–2023, and (2022–2023 average), where the inter-model spread is roughly one third of the mean magnitude. The global mean forcing is approximately half of the  $60^\circ\text{S}$ – $0^\circ$  values, reflecting the strong SH dominance of the perturbation. Over the high southern latitudes ( $60^\circ$ – $90^\circ\text{S}$ ), the mean TOA IRF is  $-0.26 \pm 0.07 \text{ W/m}^2$  over the Southern Hemisphere high latitudes, averaged from September 2022 to December 2023 average). Comparing the injection experiments, the IRF from SO2andH2O is generally comparable to SO2only at TOA, but less negative at TROP and SURF: over the  $60^\circ\text{S}$ – $0^\circ$ , TROP IRF is  $-0.32 \pm 0.13$  for SO2andH2O versus  $-0.43 \pm 0.12 \text{ W m}^{-2}$  for SO2only; at the surface, these values are  $-0.29 \pm 0.12$  versus  $-0.36 \pm 0.11 \text{ W m}^{-2}$ .

The shortwave (SW) component of the IRF follows the evolution of stratospheric AOD ( Fig. A3) but is additionally modulated by the strong seasonality of solar insolation, producing relative minima during the Austral winter. This is particularly evident at high southern latitudes (Fig. 2g–i), where the small negative SW IRF is partially offset by a positive longwave (LW) contribution. Generally, the LW signal coincides with the peak in stratospheric AOD, which, over the high southern latitudes, occurs during the Austral winter of 2023.

The SW IRF is similar between TOA and TROP but smaller in magnitude at SURF in both SO2andH2O and SO2only experiments. However, at all levels, the SW IRF is more negative in SO2andH2O during the first few months after the eruption and then becomes less negative compared to SO2only, consistent with the evolution of stratospheric AOD in the two experiments (panels j and k in Fig. A3). The differences in the net IRF between the two experiments decrease at TOA but increase at TROP due to the different LW responses to water vapor, which is slightly negative at TOA and positive at TROP.

Figure 3 provides further insight into the TOA IRF contributions from aerosols ( $IRF_{aerosol}$ ) and water vapor ( $IRF_{gas}$ ), based on analyses from WACCM6-MAM using both methods described in Section Sect. 2.2. The figure also includes a comparison of clear-sky and all-sky IRF. Among the models, WACCM6-MAM shows the strongest aerosol response (first and second columns of Fig. A4). Multiple interesting features emerge from an analyses of Fig. 3, which also includes a comparison of clear-sky and all-sky IRF.

- While the The IRF from the SO2andH2O and SO2only simulations show a consistent behavior in the late part of (black and orange lines in panel 3a) show similar behavior from late 2022 and after, significant differences (in onward. However,

substantial differences are evident during the first six months (on the order of 20%) can be found in the first six months or so (black and orange lines in panels 3a-c in WACCM6-MAM, panel 3c), with the exact duration being model dependent (Fig. A4). This is in agreement with previous works which suggested that the large quantities of water vapor favored particle growth in studies indicating that the co-injection of stratospheric water vapor promotes faster particle growth to optically efficient scattering sizes during the initial months (Zhu et al., 2022), resulting in a larger forcing. The fact that (panels a-c for SO<sub>2</sub> and H<sub>2</sub>O versus panels d-f for SO<sub>2</sub> only in Fig. A5). As a result, SO<sub>2</sub> and H<sub>2</sub>O produces a larger initial stratospheric AOD (Fig. A3 j-k) and corresponding negative radiative forcing. Later on, the forcing becomes similar later on, and shows a slight reduction due to a compensating effect: SO<sub>2</sub> only shows a larger stratospheric AOD, while SO<sub>2</sub> and H<sub>2</sub>O shows a stronger gas contribution (negative at TOA). The SO<sub>2</sub> and H<sub>2</sub>O forcing becomes slightly weaker only in the last few months of 2023, may suggest a balance between larger particles and shorter lifetime for the two cases, when the gas IRF in the two simulations becomes comparable (panel 3c).

260 – A comparison between the aerosol IRF ( $IRF_{aerosol}$ ; labeled as "Aerosol" in the figure) and the total IRF indicates that  $IRF_{aerosol}$  accounts for approximately 80% of the overall IRF response, with the remaining contribution attributed to changes in other stratospheric gases (see panel 3b vs 3a; time-averaged values are summarized in panels 3d-e).

– H<sub>2</sub>O only simulations do not show any significant forcing in clear-sky, and a more negative, but also highly variable, forcing in all-sky (blue lines in panels 3a-c). This further confirms that the water vapor forcing alone does not result in either a cooling or a warming. The small impact of stratospheric water vapor is altitude-dependent, with the largest effect occurring near the tropopause rather than at higher altitudes (Solomon et al., 2010). Indeed, stratospheric water vapor concentrations are primarily confined to the middle stratosphere (40–10 hPa) by the end of 2022, after which they rise and extend into the lower mesosphere (Millán et al., 2022; Zhuo et al., 2025). Interestingly, a comparison of the  $IRF_{gas}$  in the SO<sub>2</sub> and H<sub>2</sub>O and H<sub>2</sub>O only experiments (black and blue lines in panel 3c) suggests that the all-sky contribution is not coming from water vapor itself, but from changes to other radiatively-active gases. This will be further discussed in Section 3.3.

275 – The estimation of  $IRF_{aerosol}$  and  $IRF_{gas}$  differs depending on whether they are derived from the SO<sub>2</sub>-only and H<sub>2</sub>O-only SO<sub>2</sub> only and H<sub>2</sub>O only experiments, respectively, or from the double radiation call method applied to SO<sub>2</sub> and H<sub>2</sub>O experiment (panels 3d-e). Under both clear-sky (CS) and all-sky (AS) conditions, during the first 6 months after the eruption,  $IRF_{aerosol}$  and  $IRF_{gas}$  obtained from the SO<sub>2</sub> only and H<sub>2</sub>O only experiments, respectively, are smaller than those calculated using the double radiation call in the SO<sub>2</sub> and H<sub>2</sub>O experiment (green and red boxes, respectively). This discrepancy occurs because, in the SO<sub>2</sub> and H<sub>2</sub>O experiment, water vapor influences aerosol growth, thereby affecting  $IRF_{aerosol}$ , while any simultaneous changes in other gases (e.g. ozone) will also contribute to  $IRF_{gas}$ .

### Net Radiative Forcing at TOA - Clear-Sky

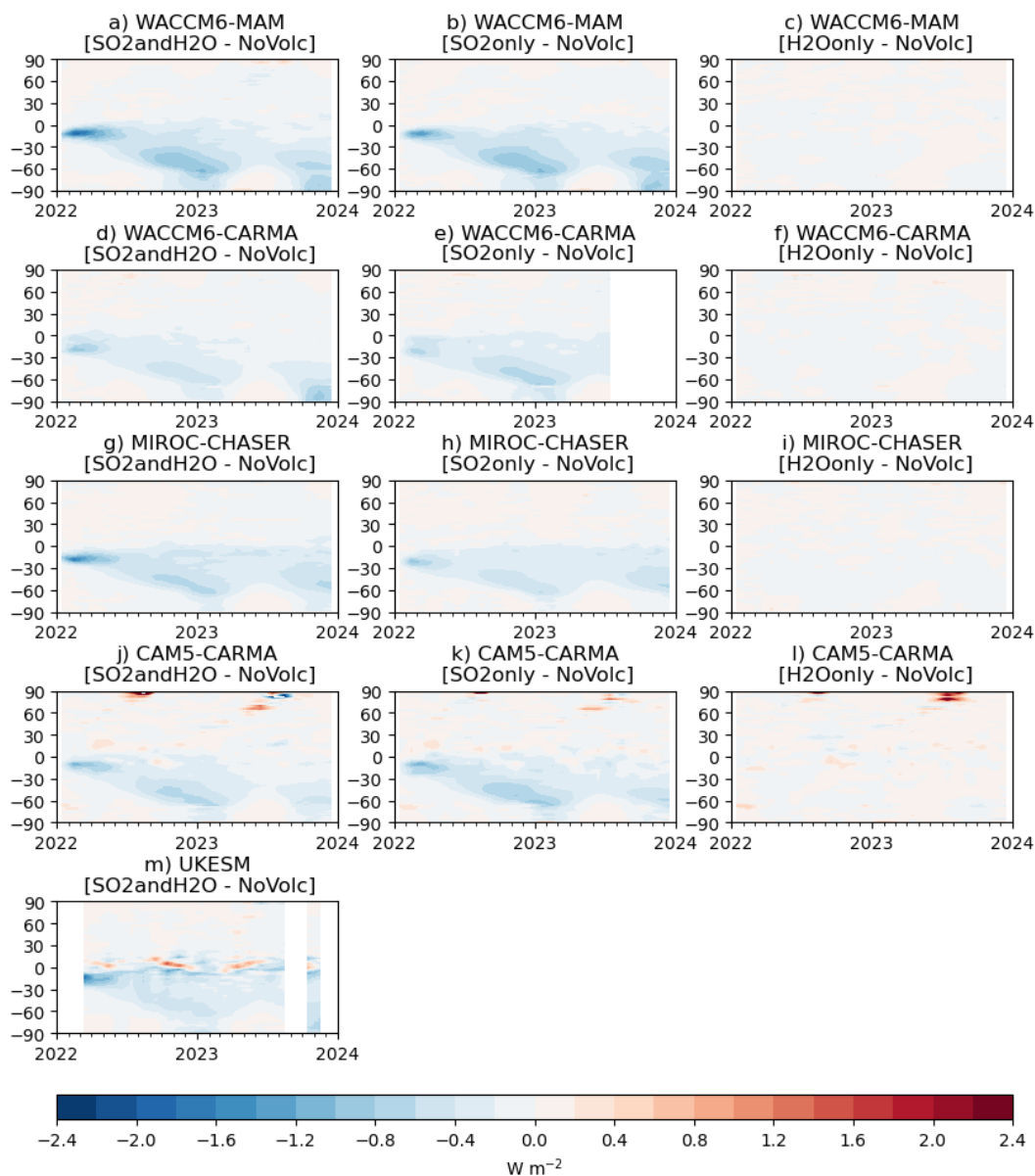


**Figure 1.** Time series of zonal mean radiative forcing at the top-of-atmosphere (TOA) under clear-sky conditions from five models: WACCM6-MAM (a–c), WACCM6-CARMA (d–f), MIROC-CHASER (g–i), CAM5-CARMA (j–l), and UKESM (m). Each column corresponds to a different perturbation scenario from the nudged experiment: the first column shows SO<sub>2</sub>andH<sub>2</sub>O, the second column SO<sub>2</sub>only, and the third column H<sub>2</sub>Oonly. [The data gap is due to missing model output for those months.](#)

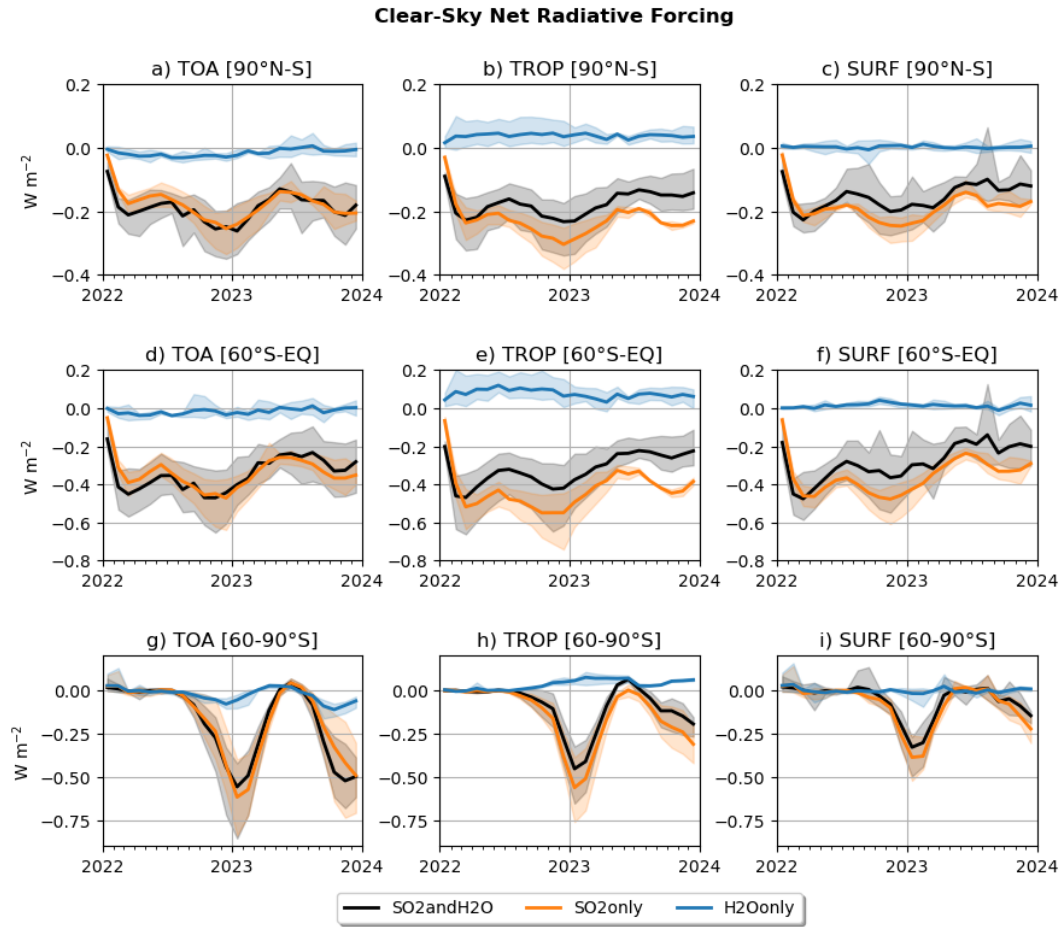


**Figure 2.** Time series of net radiative forcing under clear-sky conditions at three atmospheric levels: TOA (a, d, g), TROP (b, e, h), and SURF (c, f, i). Solid lines indicate the multi-model means for the nudged experiments as indicated in the legend, while the shaded areas represent the range (minimum to maximum) across models. Each row corresponds to a different latitudinal averaging region: the first row covers  $60^{\circ}\text{S}$  to  $90^{\circ}\text{N}$ , the second  $60^{\circ}\text{S}$  to the equator, and the third row  $60$ – $90^{\circ}\text{S}$ .

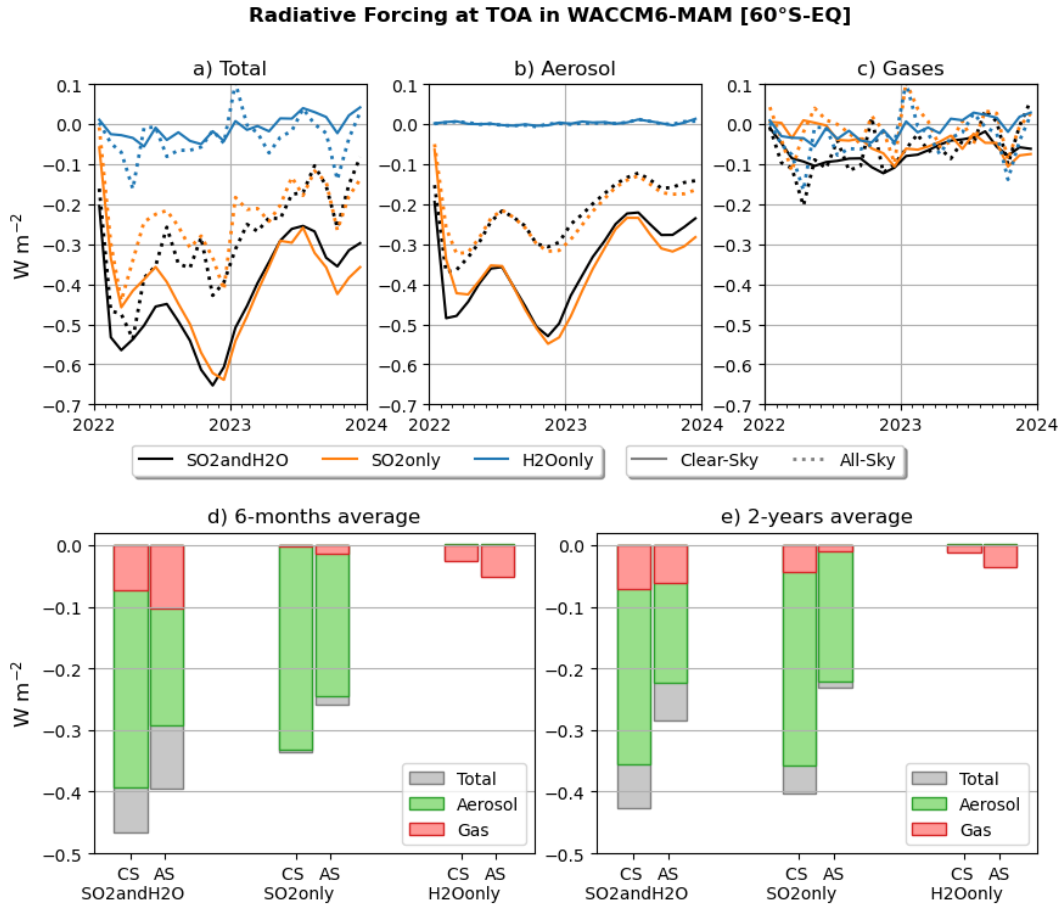


**Figure 3.** Time series of net radiative forcing at TOA, averaged between 60°S and the equator, in WACCM6-MAM. Panel (a) shows the total IRF (aerosols+gases), (b) shows the aerosol-only contribution, and panel (c) shows the gas-only contribution, all derived using the double radiation call method (see [Section Sect. 2.2](#)). Different colors indicate various nudged experiments, with solid lines representing clear-sky conditions and dotted lines indicating all-sky conditions. Panels (d) and (f) show the 6-month and 2-year averages, respectively, of the radiative forcing from the three nudged experiments, under clear-sky (CS) and all-sky (AS) conditions. The contributions from aerosols and gases alone are highlighted relative to the total forcing.

### 3.2 Comparison of the effective radiative forcing in the free running simulations

280 [Fig-Figure 4](#) shows the longer-term evolutions of the moving average forcing (calculated as  $\frac{1}{t} \int_0^t RF(t) dt$ ) in the free-running simulations with fixed climatological SSTs and sea ice (Fixed-SST). For this experiment, only two models (WACCM6-MAM and MIROC-CHASER) performed the simulations, and we show the  $\frac{1}{N_t} \sum_{i=1}^{N_t} RF_i$ , where  $N_t$  represents the number of months elapsed, and  $RF_i$  is the radiative forcing at month  $i$ . We use the moving average forcing instead of the instantaneous forcing to highlight the cumulative forcing produced by time-averaged impact of the eruption over

285 time(~~which is-~~ which provides a better measure of its overall climatic ~~impacts~~)-~~effects~~. This is shown for the free-running simulations with fixed climatological SSTs and sea ice (Fixed-SST). For this experiment, only two models, WACCM6-MAM and MIROC-CHASER, performed the simulations. The TOA ERF estimates show a very good agreement between the two models, both in terms of the overall magnitude and the rate of dissipation of the forcing, which is partly true also for the ERF estimates at the surface (see Tables A1 and A3). Larger differences between the models are present for the ERF estimates at  
290 the tropopause, whereby WACCM6-MAM shows a more negative average forcing (by  $0.1 \text{ W } \mu\text{m}^2\text{m}^{-2}$ ) in the first year (Table A2) and a different overall trend throughout the simulations.

Although the ERF response is broadly consistent between the two models, notable differences emerge in their simulated stratospheric ~~aerosol optical depth (sAOD)~~ AOD (panels 4 d and g). In particular, we observed significant discrepancies in the  
295 timing of aerosol formation and the onset of its decline. In MIROC-CHASER, stratospheric AOD starts to decline two months after the eruption, right after reaching its peak. In contrast, WACCM6-MAM shows a peak in stratospheric AOD three months post-eruption, which remains at peak levels for six months before beginning to decrease. However, the models generally agree on the ~~plume volcanic cloud~~'s southward transport, with the ~~plume volcanic cloud~~ moving towards  $60^\circ\text{S}$  after 4 to 5 months and reaching the pole by December 2023. The persistence of the aerosol ~~plume cloud~~ at low-to-mid latitudes in the SH is  
300 different between the two models, with WACCM6-MAM showing some persistence all the way to the end of 2023, whereas MIROC-CHASER show a full dissipation ~~of the cloud~~ by late 2023. ~~Contrary to sAOD~~

Contrary to the stratospheric AOD, the water vapor upward diffusion (panels 4 e and h) shows more persistence in MIROC-CHASER than WACCM6-MAM, with the latter showing no residual water vapor anomaly below 1 hPa by late 2026, whereas MIROC-CHASER shows at least 0.5 ppm more in the upper stratosphere remaining all the way to 2028. MIROC-CHASER  
305 also shows a stronger positive tropical ozone anomaly between 10 and 20 hPa compared to WACCM6-MAM, and a negative ozone anomaly higher up between 1 and 2 hPa, with the negative anomaly more persistent over time in both models (panels 4 f and i), explained by a potential enhancement of the HO<sub>x</sub>-driven loss cycle due to the water vapor anomaly (Randel et al., 2024; Fleming et al., 2024). ~~Ultimately we-~~

As with the instantaneous radiative forcing, the gas response varies depending on the atmospheric level at which it is calculated and the vertical distribution of the gases. Additionally, temperature adjustments are included here. We speculate that the stronger ~~sAOD stratospheric AOD~~ anomaly in WACCM6-MAM, ~~counterbalanced by along with~~ the stronger water vapor and ozone ~~anomaly anomalies~~ in MIROC-CHASER, ~~is the cause of the matched~~ may either offset the radiative forcing at the top of the atmosphere (TOA) or amplify it at the tropopause (TROP). This could explain the similar forcing observed in Fig. 4a -and the larger differences seen in Fig. 4b. This aspect is only further explored in Sect. 3.3 for WACCM6-MAM, where  
315 the availability of separate aerosol and gas radiative contributions allows for a clearer disentangling of each factor.

In Fig. 4 we also provide a comparison with available observations, with more in depth comparisons ~~also provided~~ presented in Zhuo et al. (2025). In ~~particular we use the Global Space-based Stratospheric Aerosol Climatology version 2.22 (GloSSAC, NASA/LAR for zonal-mean monthly-mean stratospheric aerosol optical depth and the Stratospheric Water and Ozone Satellite Homogenized~~

320 ~~dataset version 2.6 (SWOOSH, Davis et al., 2016) for H<sub>2</sub>O.~~ In general, both models show good qualitative agreement with  
observations: ~~while the observations. While~~ GloSSAC does not see the high peak at the beginning of the eruption, transport  
~~towards the SH happens on the same timescales as the simulated one~~ capture the pronounced peak immediately following  
the eruption, which is evident in other observational datasets discussed in Zhuo et al. (2025), this mainly reflects the limited  
spatiotemporal coverage of the SAGE III/ISS observations on which GloSSAC is based during the earliest post-eruption phase.  
325 Despite this limitation, transport toward the Southern Hemisphere occurs on similar timescales in both the observations and  
the simulations, with WACCM6-MAM showing a better match in terms of ~~residual aerosol plume at the residual aerosol cloud~~  
around 60°S. In terms of H<sub>2</sub>O, models generally reproduce the upward transport pattern; however, SWOOSH consistently re-  
ports higher values. As also noted in ~~(Zhuo et al., 2025)~~ Zhuo et al. (2025), the comparison between models and observations is  
330 primarily aimed at assessing transport patterns, since anomalies are derived differently in each case, requiring careful consider-  
ation for a meaningful quantitative comparisons. In the following section, we will discuss how the results for WACCM6-MAM  
compare between fully coupled and nudged simulations.

**Table 3.** Effective radiative forcing (in  $\text{W m}^{-2}$ ) at the Top of Atmosphere under clear-sky conditions. Forcing is averaged between 60°S and the equator.

Model	6 Months	1 Year	2 Years	5 Years	10 Years
WACCM6-MAM	$-0.31 \pm 0.14$	$-0.36 \pm 0.14$	$-0.27 \pm 0.14$	$-0.12 \pm 0.14$	$-0.07 \pm 0.06$
MIROC-CHASER	$-0.30 \pm 0.17$	$-0.35 \pm 0.11$	$-0.24 \pm 0.12$	$-0.14 \pm 0.10$	$-0.04 \pm 0.05$

### 3.3 Further exploration of radiative forcings in WACCM6-MAM

In this section we show a comparison of radiative forcings in the three different experiments, which only WACCM6-MAM  
 335 conducted in full. This comparison provides useful insights to the different ways to define the radiative impacts of the **plume**  
volcanic cloud between RF, ERF and IRF.

~~Fig. ?? shows~~ Figure 5 shows that, across all experiments and at the three atmospheric levels, the simulated clear-sky radiative forcing is negative and locally statistically significant in the Southern Hemisphere during the first two years after following  
 340 the eruption. The sign, as well as the spatial and temporal evolution, is consistent across the different model configurations and atmospheric levels considered. ~~The differences in stratospheric aerosol optical depth change (sAOD, Fig. A8 a-c) among the experiments are negligible: as discussed in past works, this indicate that atmospheric nudging does not necessarily improve the residual stratospheric circulation (Chrysanthou et al., 2019). However~~ However, when including the atmospheric temperature adjustments ~~(as is the case in the free running simulations)~~ in Fixed-SST and the ocean response in Coupled, the radiative  
 345 forcing from aerosols and water vapor is ~~markedly substantially~~ markedly substantially smaller than in the nudged simulation. ~~The clear-sky IRF at TOA averaged over the southern hemisphere~~, particularly at TOA. This difference is more evident when averaging over the Southern Hemisphere (60°S to the equator), as shown in Fig. 6.

In panel 6a, the clear-sky IRF at TOA during the first 2 years after the eruption is  $-0.43 \text{ W m}^{-2}$  in the nudged simulations, whereas in the free running experiments it is  $-0.27 \text{ W m}^{-2}$  in both the coupled ocean and atmosphere-only cases. ~~Despite~~  
 350 ~~being~~ Although smaller than in the nudged simulations, ~~such a response is still outside these responses remain outside the range~~ of natural variability, which ~~we calculate is estimated~~ in Fig. ?? 6 as one standard deviation in from the control ensemble (NoVolc). In general, while most of the results presented here are for the SH only, when considering global mean the values are reduced by approximately half, reaching a value of  $-0.09 \text{ W m}^{-2}$  at the TOA for the Coupled experiment in 2022-2023, which falls within the range of natural variability (see Fig. A7 and Table 4).

~~When distinguishing the contribution from aerosol and gas-radiation interaction in Fig. ??, the~~ The reduced net radiative forcing relative to the nudged case arises from the inclusion of temperature and ozone adjustments. Indeed, differences in the simulated stratospheric AOD changes among the experiments are negligible (Fig. A8a-c), consistent with previous studies showing that atmospheric nudging does not necessarily improve the representation of the residual stratospheric circulation

(Chrysanthou et al., 2019). Instead, the response is largely dominated by gas-driven variability, which is strongest in the  
360 Coupled experiment and includes a late-period negative radiative forcing at TOA in the first 2 years results from the negative  
in 2025 that is not present in the other simulations (Fig. 6a-b).

The separation of aerosol–radiation and gas–radiation contributions to the total radiative forcing (Fig. 7) shows that the  
negative TOA forcing during the first two years following the eruption is primarily driven by the aerosol contribution from  
365 Hunga aerosols, and a residual, partially offset by a positive contribution from changes in gases (contrasting with the negative  
gas–radiation interaction forcing seen in the nudged simulations). This behavior contrasts with the nudged simulations, where  
the gas–radiation interaction produces a negative forcing (Fig. 3). Notably, in the free-running simulations. In the free-running  
simulations, the gas contribution to radiative forcing is significantly affected is strongly influenced by natural variability (red  
line in Fig. ??), in particular 7), particularly for all-sky RF, which hinders a confident determination of the RF response without  
370 the use of a large ensembles radiative forcing, which limits the detectability of the forced response without large ensemble  
sizes (Fig. A9). Moreover, in-

In the second half of 2025, as the sAOD in the tropics tropical stratospheric AOD returns to background levels (Fig. A8a–c),  
only the coupled Coupled experiment exhibits a significant negative radiative forcing in the Tropics at both the tropics at both  
TOA and TROP, reaching with magnitudes comparable to those observed during the first post-eruption year (Fig. ??6a and b),  
375 while the forcing at the SURF becomes positive. Such radiative forcing change in 2025 in the coupled This late-period forcing  
in the Coupled experiment is primarily driven by gas–radiation gas–radiation interactions, with significant negative clear-sky  
values seen emerging in 2025 (Figure ??Fig. 7c).

Changes in gas radiative interactions can be important contribution to the overall RF, and these are the result of not just the  
380 Hunga induced changes in The gas radiative forcing results not only from Hunga-induced changes in stratospheric water vapor  
(which are similar across the three cases), but also experiments; Fig. A8d–f) but also from changes in stratospheric temper-  
atures and ozone, as well as any associated changes in dynamics (as these modulate the temperatures and ozone, in particular  
in associated dynamical adjustments that modulate both, particularly in the lower stratosphere). By definition, the nudged  
simulation do not include any changes in temperatures or dynamics. While free running simulations include these components,  
385 the fully coupled simulation includes additional forcing from changes in the ocean variability. Differences in the gas radiative  
interactions and gas RF between the nudged and coupled simulations could be partly explained by the associated changes  
in stratospheric temperatures and ozone. These contributions are further explored in Fig. 8. The gas–radiation interaction  
is dominated by the LW component (Fig. 8a–c), with differences among the atmospheric configurations driven primarily by  
temperature and dynamical responses: Zhuo et al. (2025) has shown an upper-level cooling due to the water vapor and a lower  
390 stratospheric level warming from LW absorption from the sulfate aerosols. The decrease in upper stratospheric temperatures  
in the free-running simulations in the free-running simulations.

During the first two years following the eruption, the TOA gas radiative forcing is positive in the Coupled simulation, more  
variable in Fixed-SST, and negative in the Nudged case (Fig. A8j and Fig. ??d) caused by higher water vapor at the same

level, likely results in an initial positive RF at the TOA (8a-c). This behavior reflects the combined effects of increased water vapor in the middle stratosphere and reduced ozone in the lower stratosphere. When temperature and dynamical changes are excluded, as in the Nudged simulation, the water vapor increase and ozone decrease (black curves in Fig. 8f and i) enhance outgoing LW radiation at TOA, resulting in a negative forcing. In contrast, when temperature adjustments are included, as in the Coupled and Fixed-SST simulations, the cooling at higher altitudes where water vapor anomalies peak (black curves for water vapor and red curves for temperature in Fig. 8d and e) reduces outgoing LW radiation, yielding a positive TOA forcing during the first two post-eruption years. Furthermore, the fully coupled simulations show a distinct pattern of increasing tropical lower stratospheric ozone in the first two years and decreasing ozone in 2025. Since Coupled shows a distinct evolution in the tropical lower stratosphere, characterized by increased ozone and warming during 2022–2023, followed by decreased ozone and cooling in 2025 (panel 8g). Because ozone in the lower stratosphere acts as a greenhouse gas, this contributes to the positive RF in these changes contribute to an additional positive radiative forcing during the first two years and to a negative RF a negative forcing in 2025 (Fig. A8g and Fig. ??g)., when water vapor anomalies have largely returned to background levels. The close correlation of changes in ozone and temperatures in this region, not seen in Fixed-SST (panel 8h), is strongly indicative of their dynamical origin, suggesting an associated decrease in tropical upwelling in 2022–2023 and increase in 2025.

As discussed in (Bednarz et al., 2025), the coupled ocean WACCM6-MAM simulations shows a significant modulation of the ENSO–El Niño–Southern Oscillation (ENSO) variability by the eruption, with La-Nina like response in 2022–2023 and an El-Nino like response in 2025. In general, ENSO is an important driver of interannual variability in tropical upwelling, which modulates lower stratospheric in turn modulates lower-stratospheric temperatures and ozone (Randel et al., 2009), and can therefore exert an important a substantial influence on the overall RF radiative forcing.

In general, while most of the results presented here are for the SH only, when considering global mean the values are reduced by approximately half, reaching a value of  $-0.09 \text{ W/m}^2$  at the TOA for the Coupled experiment in 2022–2023, which falls within the range of natural variability (see Fig. A7 and Table 4), and corresponds to an average sAOD of 0.005 over the same period.

Changes with Fixed SST [SO<sub>2</sub>andH<sub>2</sub>O - NoVolc] [60°S-EQ]

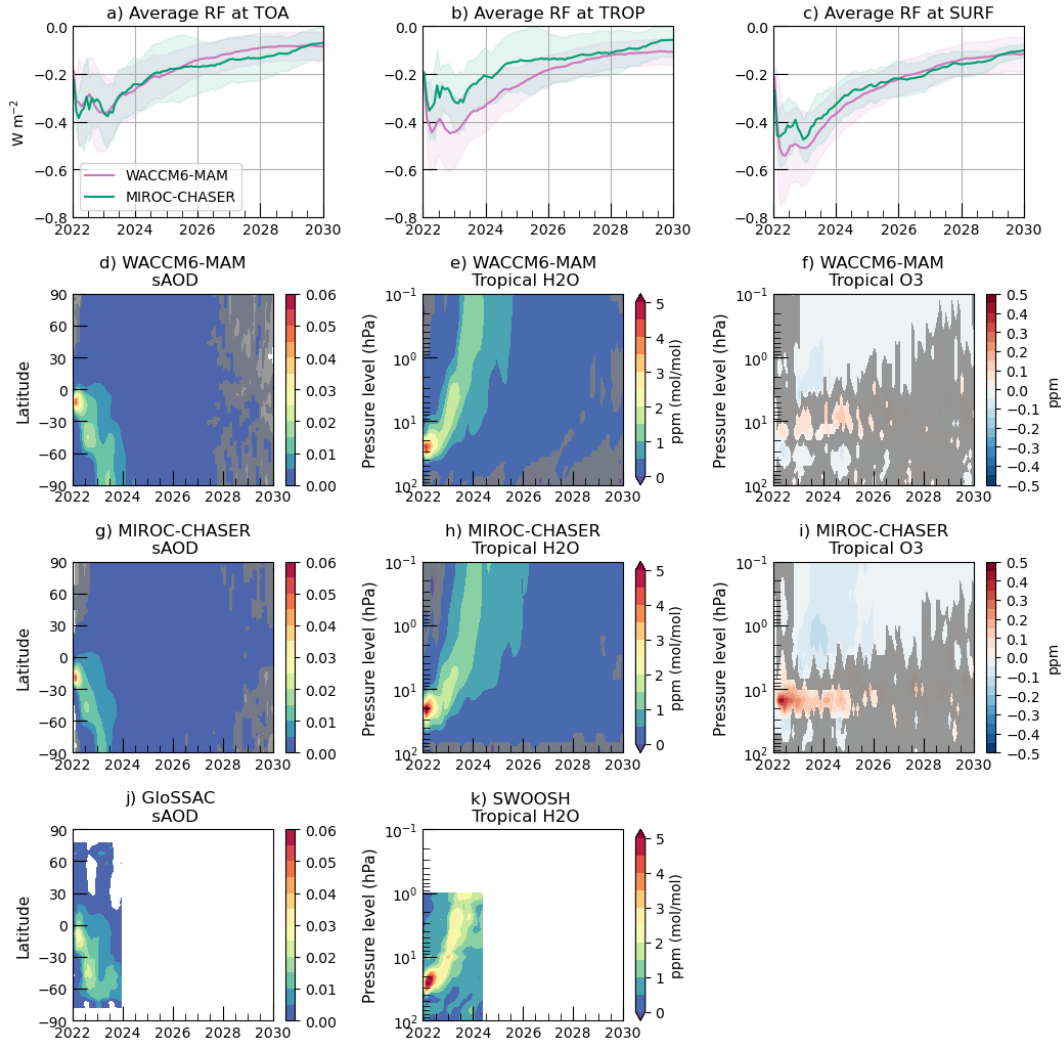


**Figure 4.** a-c) Timeseries-Time series of moving average of effective radiative forcing (ERF) under clear-sky conditions, averaged between 60°S and the equator, from the free running simulations with fixed climatological SSTs and sea ice (Fixed-SST). ERF is shown at TOA, TROP, and SURF for WACCM6-MAM and MIROC-CHASER. Solid lines represent the ensemble mean, and shaded areas represent  $\pm 1$  standard deviation across ensemble members. Each shaded area uses the same color as the line representing that model, as shown in the legend. Zonal mean of changes in stratospheric aerosol optical depth (sAOD) for WACCM6-MAM, MIROC-CHASER and GloSSAC (d, g, j), tropical (30°S-N) H<sub>2</sub>O mixing ratio for WACCM6-MAM, MIROC-CHASER and SWOOSH (e, h, k) and O<sub>3</sub> mixing ratio for WACCM6-MAM and MIROC-CHASER (f and i). Changes are calculated as the difference between perturbed and unperturbed simulations for the models, and relative to the 2005–2021 climatology period for the observations. Gray areas indicate regions where the differences are not statistically significant at the 5% level based on Student’s t-test.

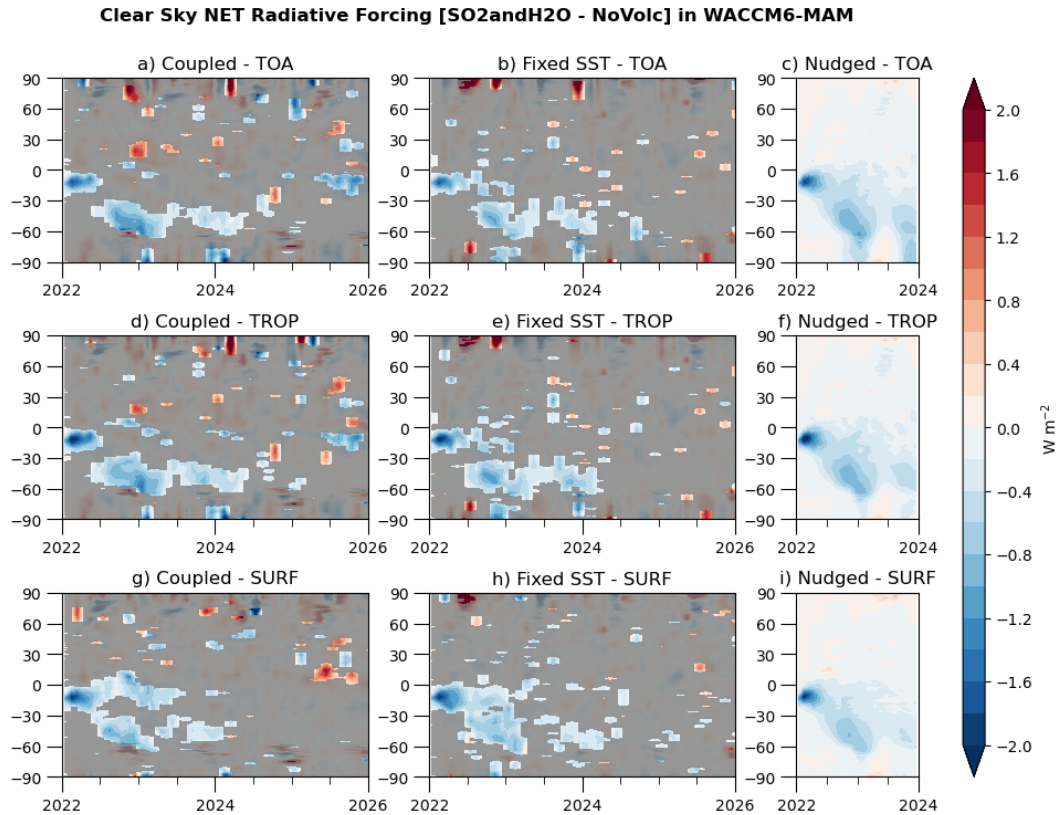


**Figure 5.** Time series of zonal mean radiative forcing under clear-sky conditions for SO<sub>2</sub>andH<sub>2</sub>O experiment in WACCM6-MAM, at TOA (a-c), TROP (d-f), and SURF (g-i). Each column represents a different model setup: first and second columns are free running experiments with either coupled ocean or climatological sea surface temperatures and sea ice (Coupled and Fixed-SST, respectively), third column indicates nudged simulations (Nudged). Results from Fixed-SST and Coupled are ensemble means over all 30 members. Gray areas indicate regions where the differences are not statistically significant at the 5% level based on Student's t-test.

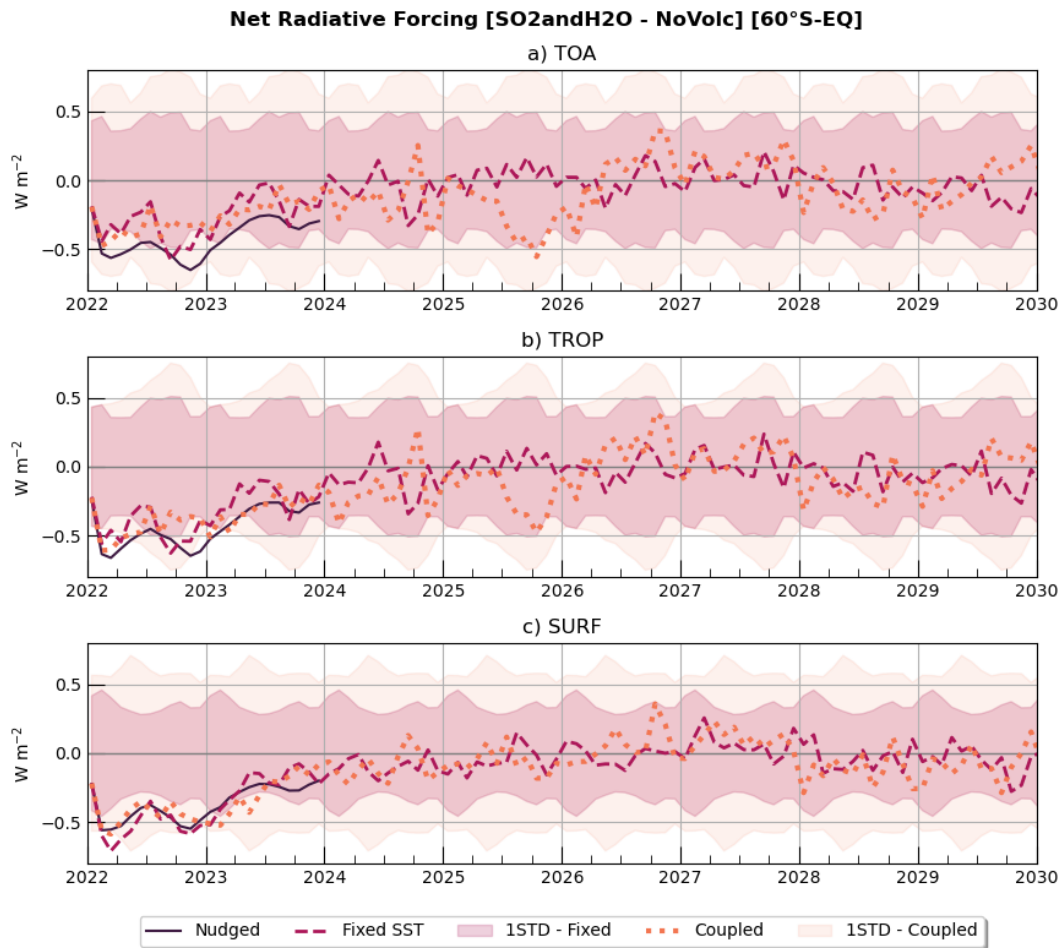


**Figure 6.** Time series of net radiative forcing under clear-sky conditions between 60°S and the equator for SO<sub>2</sub>andH<sub>2</sub>O experiment in WACCM6-MAM at TOA (a), TROP (b), and SURF (c). Solid lines indicate the results form nudged simulations, dashed lines from the free running simulations with fixed climatological SSTs and sea ice and dotted lines from the coupled experiment. Shading indicates the monthly internal variability, calculated as 1 standard deviation over 10-year simulations using a 30-member ensemble from the unperturbed NoVolc experiment.

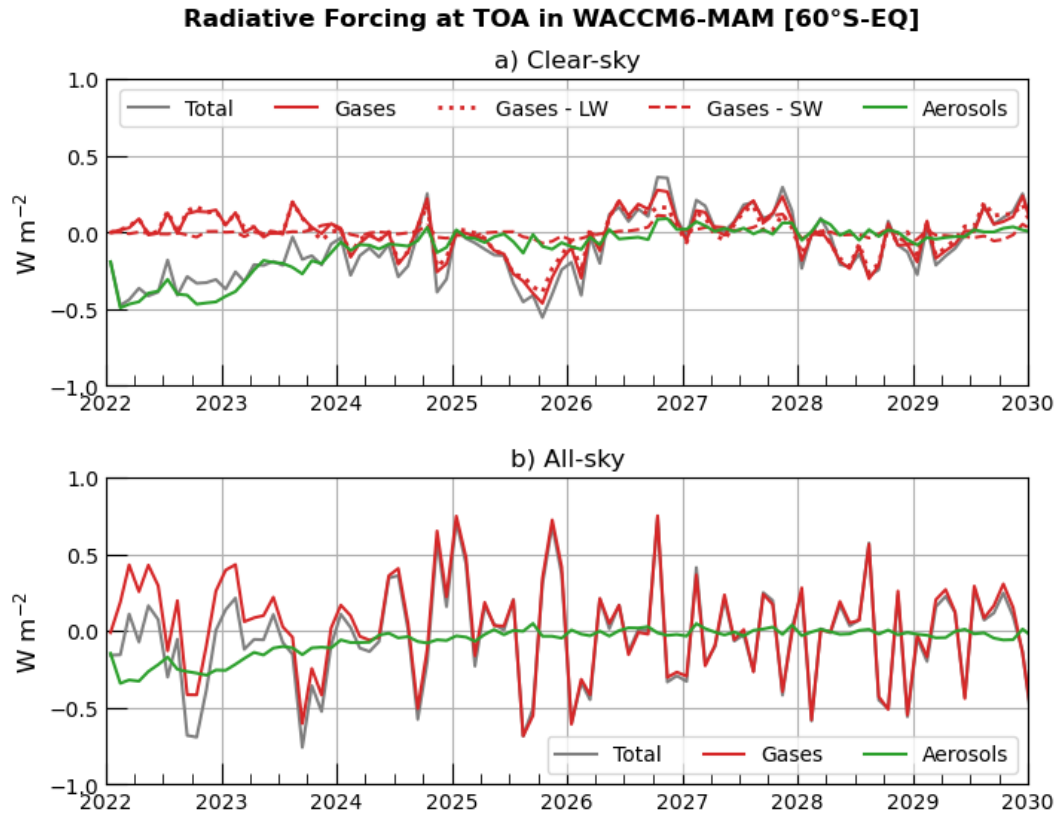


**Figure 7.** Time series of net radiative forcing at TOA for the SO<sub>2</sub>andH<sub>2</sub>O fully coupled experiment in WACCM6-MAM. RF is averaged between 60°S and the equator and calculated in Clear-sky and All-Sky conditions (a-b, respectively). Different colors indicate the total radiative forcing (gray), the aerosol-only contribution (green), and the gas-only contribution (red). Red line styles distinguish the net forcing (solid), the shortwave (SW) component (dashed), and the longwave (LW) component (dotted).

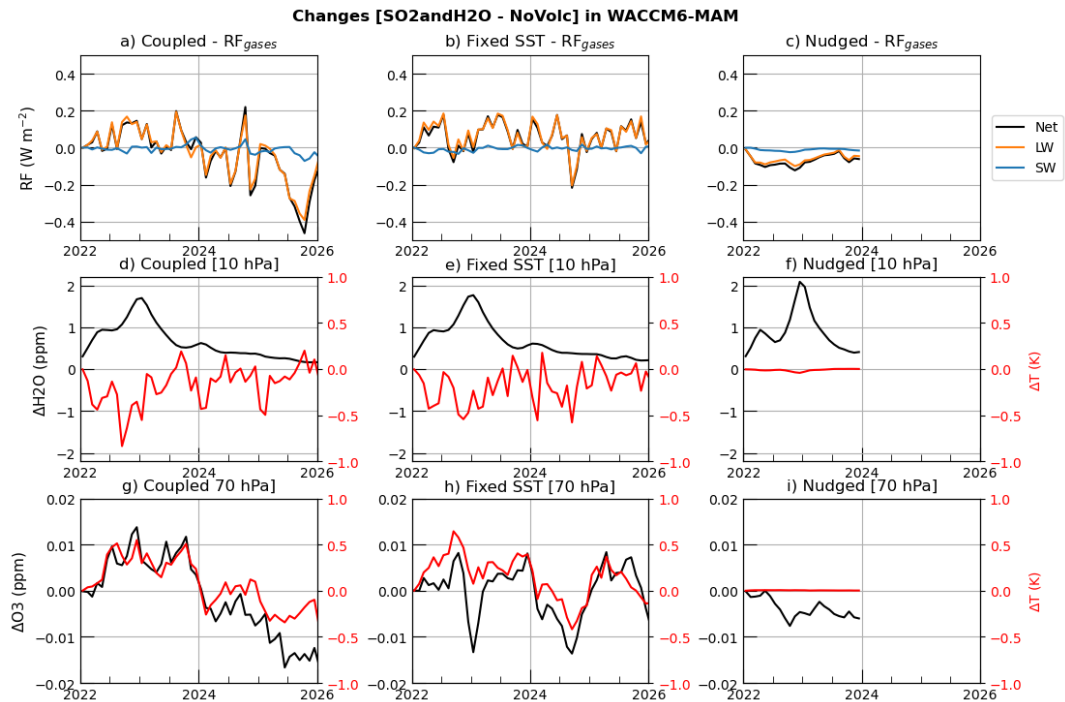


**Figure 8.** Time series of net, shortwave (SW), and longwave (LW) gas-radiation interaction RF (sAOD; panels a–c), tropical H<sub>2</sub>O concentrations and tropical temperature at 10 hPa (30°S–30°N; panels d–f, in ppm and K, respectively), and tropical O<sub>3</sub> concentrations and tropical temperature at 70 hPa (30°S–30°N; panels g–i, in ppm and K, respectively). Changes are computed as the difference between the SO<sub>2</sub>andH<sub>2</sub>O and NoVolc experiments for the (a, d, g) Coupled, (b, e, h) Fixed-SST, and (c, f, i) Nudged configurations.

**Table 4.** Radiative forcing (in  $W/m^2$ ) at the Top of Atmosphere under clear-sky conditions in WACCM6-MAM. Forcing is averaged between 60°S and the equator and calculated over 2022-2023.

	Coupled (60S/Eq)	Coupled (global)	Fixed-SST (60S/Eq)	Fixed-SST (global)	Nudged (60S/Eq)	Nudged (global)
TOA	$-0.27 \pm 0.24$	$-0.09 \pm 0.16$	$-0.27 \pm 0.11$	$-0.16 \pm 0.09$	-0.43	-0.24
TROP	$-0.37 \pm 0.18$	$-0.15 \pm 0.09$	$-0.34 \pm 0.11$	$-0.20 \pm 0.09$	-0.44	-0.25
SURF	$-0.36 \pm 0.13$	$-0.19 \pm 0.09$	$-0.37 \pm 0.10$	$-0.23 \pm 0.09$	-0.37	-0.20

Time series of zonal mean changes in stratospheric aerosol optical depth (sAOD; panels a–e), tropical stratospheric H<sub>2</sub>O concentrations (30S–30N; panels d–f, in ppm), tropical stratospheric O<sub>3</sub> concentrations (30S–30N; panels g–i, in ppm), and tropical stratospheric temperature (30S–30N; panels j–l, in K). Changes are computed as the difference between the SO<sub>2</sub> and H<sub>2</sub>O and NoVolc experiments for the (a, d, g, j) Coupled, (b, e, h, k) Fixed-SST, and (c, f, i, l) Nudged configurations. Gray areas indicate regions where the differences are not statistically significant at the 5% level based on Student’s t-test.

Time series of net radiative forcing under clear-sky conditions between 60°S and the equator for SO<sub>2</sub> and H<sub>2</sub>O experiment in WACCM6-MAM at TOA (a), TROP (b), and SURF (c). Solid lines indicate the results from nudged simulations, dashed lines from the free running simulations with fixed climatological SSTs and sea ice and dotted lines from the coupled experiment. Shading indicates the monthly internal variability, calculated as 1 standard deviation over 10-year simulations using a 30-member ensemble from the unperturbed NoVolc experiment.

Time series of net radiative forcing at TOA for the SO<sub>2</sub> and H<sub>2</sub>O fully coupled experiment in WACCM6-MAM. RF is averaged between 60°S and the equator and calculated in Clear-sky and All-Sky conditions (a–b, respectively). Different lines represent the total RF and each contribution from aerosols only and gases only.

## 4 Conclusions

In this work we have provided the first multi-model analyses of the radiative impacts of the Hunga Tonga-Hunga Ha’apai volcanic eruption, which co-injected large amounts of water vapor and a small-to-moderate amount of SO<sub>2</sub> into the stratosphere. Our multi-model results confirm previous analyses from Zhu et al. (2022) and Stenchikov et al. (2025), Stenchikov et al. (2025) and (Sellitto et al., 2025) which indicated a potential net negative forcing from the volcanic plume cloud, due to the formation of a persistent layer of stratospheric sulfate aerosol whose sizes were larger (and thus exerted a stronger cooling effect) than expected based on past explosive eruptions, due to microphysical growth driven by the unusually large amounts of water vapor that rapidly grew to optically efficient sizes, enhancing shortwave scattering relative to background conditions.

In particular, our analysis indicates a global mean effective radiative forcing at the top of the atmosphere of  $-0.14 \pm 0.10 W/m^2$ , based on the multi-model mean from free-running simulations with fixed sea surface temperatures. If the averaging is

440 restricted to the Southern Hemisphere, these values nearly double, highlighting the hemispheric asymmetry in the distribution of the aerosol ~~plume-cloud~~ and its radiative impact. When coupled with the ocean, the global forcing is smaller and more noisy ( $-0.09 \pm 0.16 \text{ W /m}^2\text{m}^{-2}$ ), due to the eruption's significant modulation of ENSO variability, triggering a La Niña-like response in 2022–2023 and an El Niño-like response in 2025 (Bednarz et al., 2025), which, in turn, impacts tropical upwelling and alters lower stratospheric ozone in the tropics. However, the predominant effect arises from the sulfate aerosols ( $-0.18 \pm$   
445  $0.02 \text{ W /m}^2\text{m}^{-2}$ , IRF from the multi-model mean in the Nudged SO<sub>2</sub>only) and only a marginal contribution from the water vapor. The two methods used to estimate the IRF from aerosol-radiation and gas-radiation interactions, one simulating separate injections of SO<sub>2</sub> and water vapor, and the other employing a double radiation call for their co-injection, reveal biases in IRF calculations. Our results provide useful insight that can be used to inform future climate assessments (Forster et al., 2025) that aim to identify the contributions of the single natural and anthropogenic factors to global radiative imbalance and temperatures.

450

It is important to note that in the simulations analyzed in this work, a value of 0.5 Tg of SO<sub>2</sub> was used (Zhu et al., 2025). Analyses by Sellitto et al. (2024), using the Infrared Atmospheric Sounding Interferometer (IASI), however, suggest that the overall SO<sub>2</sub> burden from the Hunga eruption was larger than what Carn et al. (2022) estimated using UV measurements from the Ozone Monitoring Instrument (OMI) on NASA's Aura satellite, with a lower limit of 1.0 Tg. This suggests that the  
455 results ~~we~~ presented here might be underestimated, if higher retrieval estimates for the sulfate ~~aerosol~~ burden were confirmed. particularly in light of the uncertainties in stratospheric AOD retrievals highlighted by comparisons between the GloSSAC and OMPS-LP datasets in Zhuo et al. (2025).

In general, ~~aerosol optical depth (AOD) AOD~~ is often assumed to scale linearly with radiative forcing, especially in the stratosphere, meaning that a doubling of AOD would typically result in a doubling of negative radiative forcing. However,  
460 this relationship depends not only on the total aerosol burden but also on the particle size distribution ~~A larger burden does not necessarily lead to a proportionally larger AOD, as the (Sellitto et al., 2025), as~~ AOD is highly sensitive to particle size ~~However, our analyses also show that the water vapor contribution to the sulfate forcing is significant, suggesting that even a doubling of the burden might not necessarily have resulted in a doubling of the negative forcing. Furthermore, our analysis shows~~ Consequently, an increased aerosol burden does not necessarily translate into a proportionally larger AOD or radiative forcing.

465

Our analyses further indicate that stratospheric water vapor ~~significantly contributes to~~ plays a significant role in the initial growth of sulfate aerosols and thus in modulating the aerosol-radiation interaction. Results from nudged WACCM6-MAM simulations ~~indicate show~~ that, during the first six months following the eruption, the aerosol-radiation interaction IRF in the Southern Hemisphere would be over 10% smaller ( $-0.34 \text{ W /m}^2\text{m}^{-2}$  vs  $-0.39 \text{ W /m}^2\text{m}^{-2}$ ) if the co-injection of water vapor is  
470 not included. ~~However~~

As a result, even if the sulfate aerosol burden were doubled, non-linearities in the AOD-forcing relationship would likely be less than double. Ultimately, the higher-enhanced particle scattering efficiency and longer atmospheric lifetime following the Hunga eruption - attributed to its higher injection altitude and increased co-emission of water vapor (Li et al., 2024) - help ~~s~~ explain why an SO<sub>2</sub> injection at least 20 times smaller than Pinatubo (10-12 Tg; Ukhov et al., 2023) resulted in an ~~sAOD~~

475 stratospheric AOD only about 10 times lower ~~and thus capable of having~~, yet still capable of exerting a small but ~~nonetheless~~ non-negligible ~~contribution on the overall Earth~~ impact on Earth's radiative balance over ~~the following year~~.

## Appendix A: Figures and tables

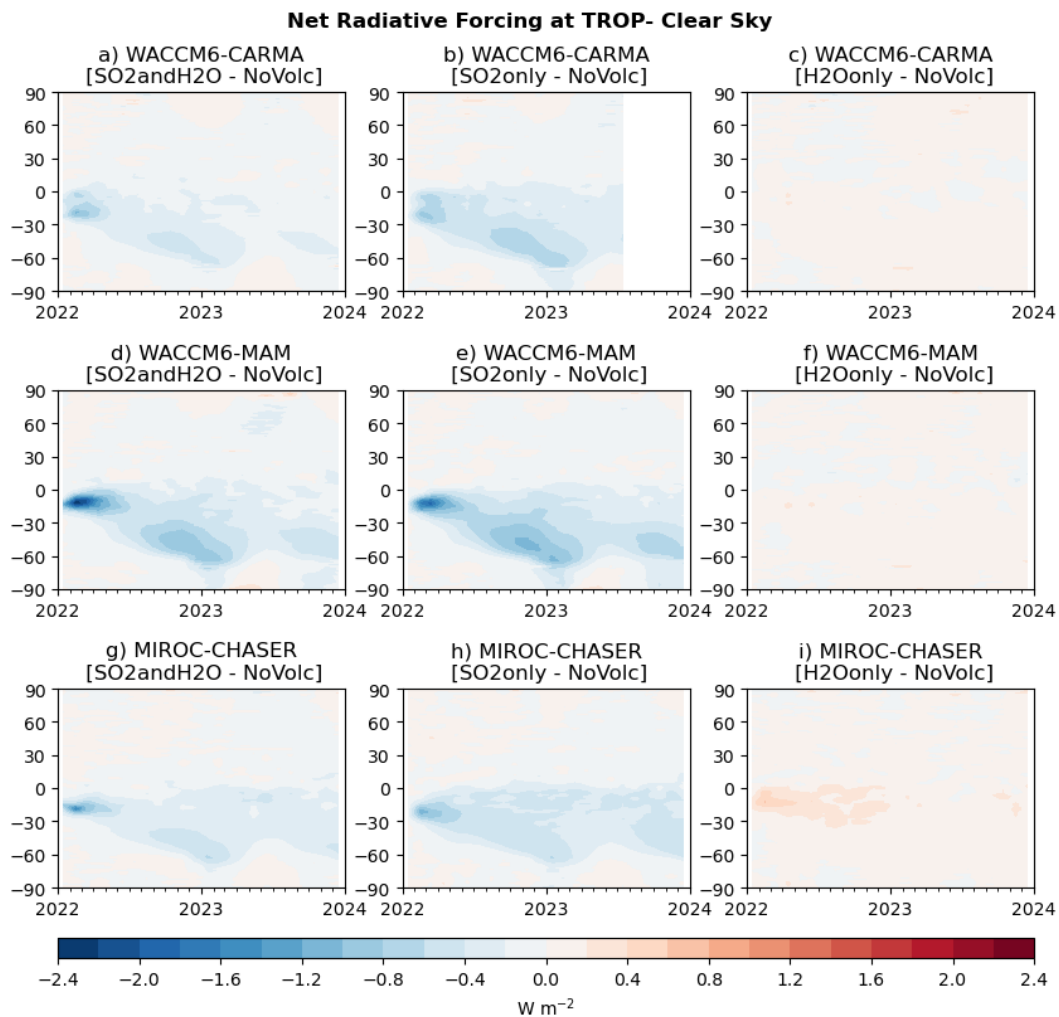


**Figure A1.** Time series of zonal mean radiative forcing at the tropopause (TROP) under clear-sky conditions from three models: WACCM6-CARMA (a–c), WACCM6-MAM (d–f), and MIROC-CHASER (g–i). Each column corresponds to a different perturbation scenario from the nudged experiment: the first column shows SO<sub>2</sub>andH<sub>2</sub>O, the second column SO<sub>2</sub>only, and the third column H<sub>2</sub>Oonly.

### Net Radiative Forcing at SURF- Clear Sky

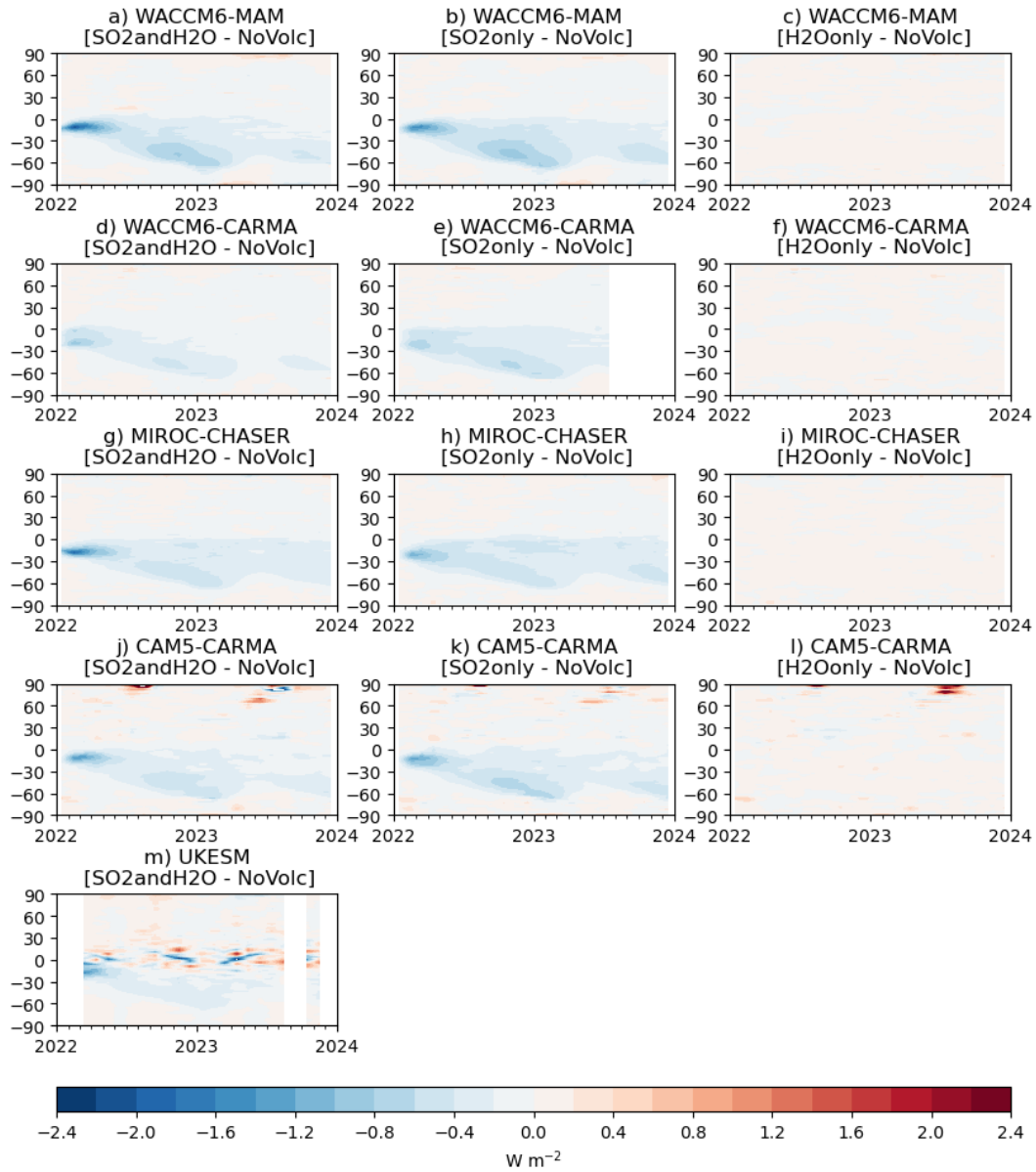


**Figure A2.** Time series of zonal mean radiative forcing at the surface (SURF) under clear-sky conditions from three models: WACCM6-MAM (a–c), WACCM6-CARMA (d–f), MIROC-CHASER (g–i), CAM5-CARMA (j–l), and UKESM (m). Each column corresponds to a different perturbation scenario from the nudged experiment: the first column shows SO<sub>2</sub>andH<sub>2</sub>O, the second column SO<sub>2</sub>only, and the third column H<sub>2</sub>Oonly.

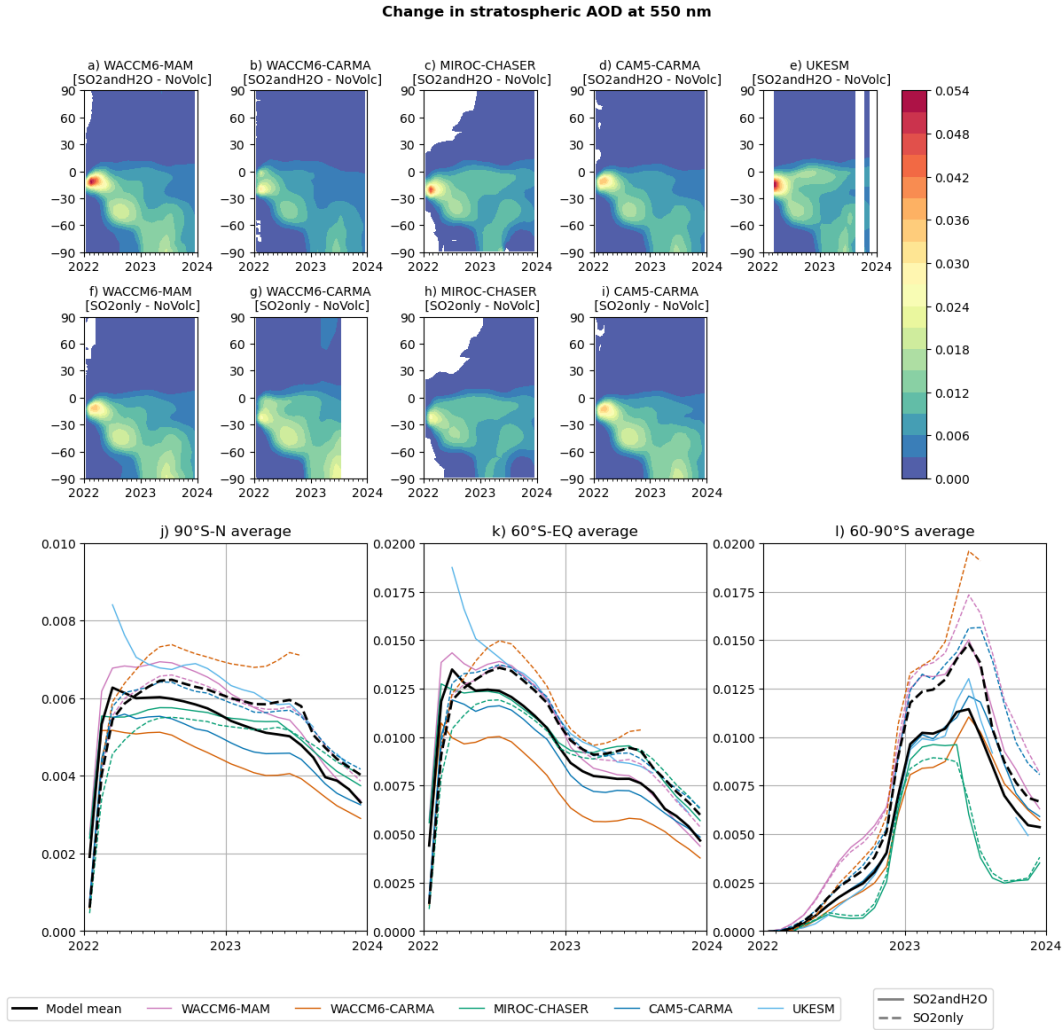


**Figure A3.** Time series of zonal mean stratospheric aerosol optical depth anomalies (perturbed minus control) from five models: WACCM6-MAM (a, f), WACCM6-CARMA (b, g), MIROC-CHASER (c, h), CAM5-CARMA (d, i), and UKESM (e). The first two rows correspond to perturbation scenarios from  $SO_2andH_2O$ , and the second row shows  $SO_2only$ . The third row includes regional averages of the same quantity for two latitude bands: 90°S-N (j), 60°S–equator (k) and 60–90°S (l).

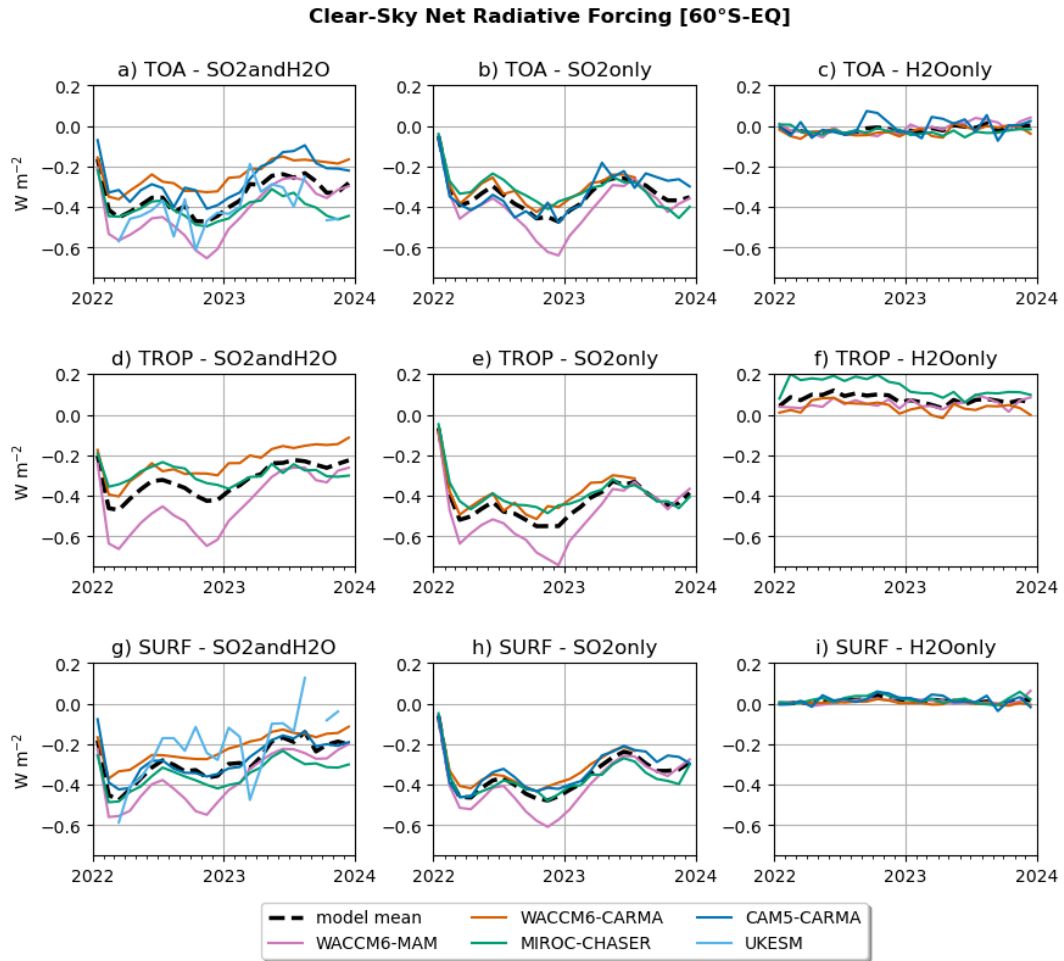


**Figure A4.** Time series of net radiative forcing under clear-sky conditions at three atmospheric levels: TOA (a, d, g), TROP (b, e, h), and SURF (c, f, i). Each column corresponds to a different perturbation scenario from the nudged experiment: the first column shows SO<sub>2</sub>andH<sub>2</sub>O, the second column SO<sub>2</sub>only, and the third column H<sub>2</sub>Oonly. The black dashed line represents the multi-model mean, each model is represented with a different color.

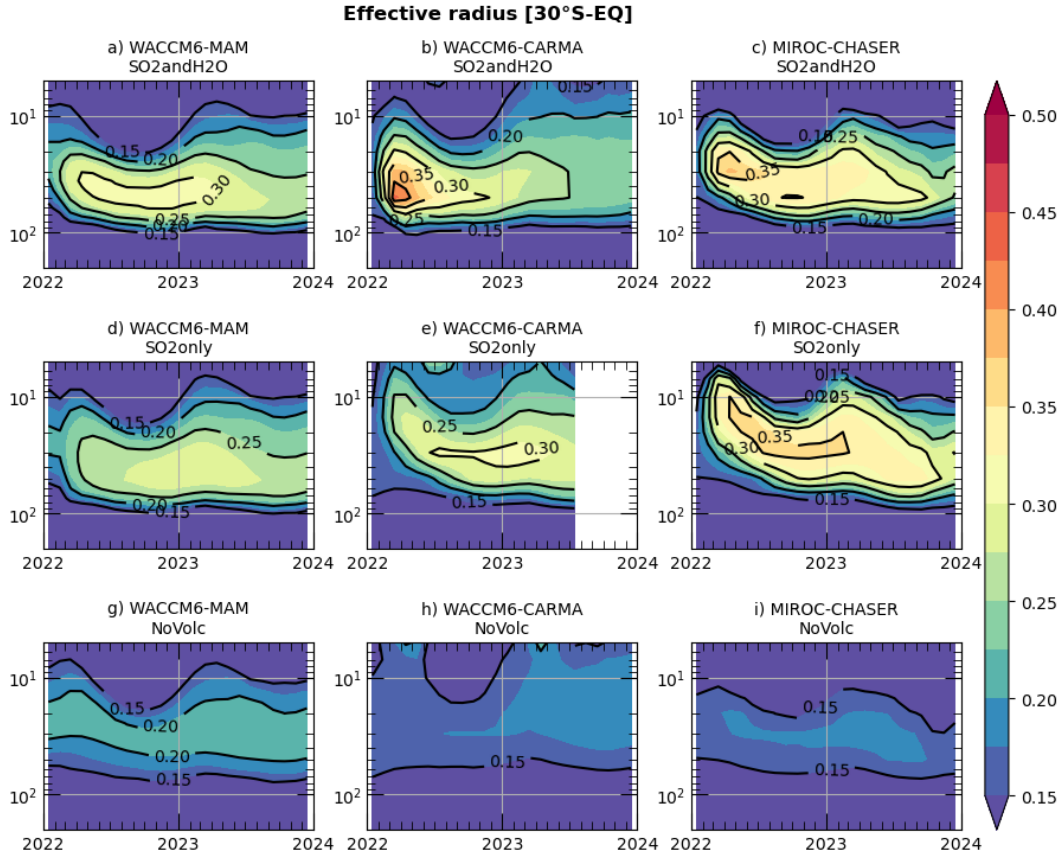


**Figure A5.** Time series of effective radius averaged over 30°S and the equator for (a, d, g) WACCM6-MAM, (b, e, h) WACCM6-CARMA, and (c, f, i) MIROC-CHASER. Each row corresponds to a different scenario from the nudged experiment: the first column shows SO<sub>2</sub>andH<sub>2</sub>O, the second column SO<sub>2</sub>only, and the third column NoVolc.

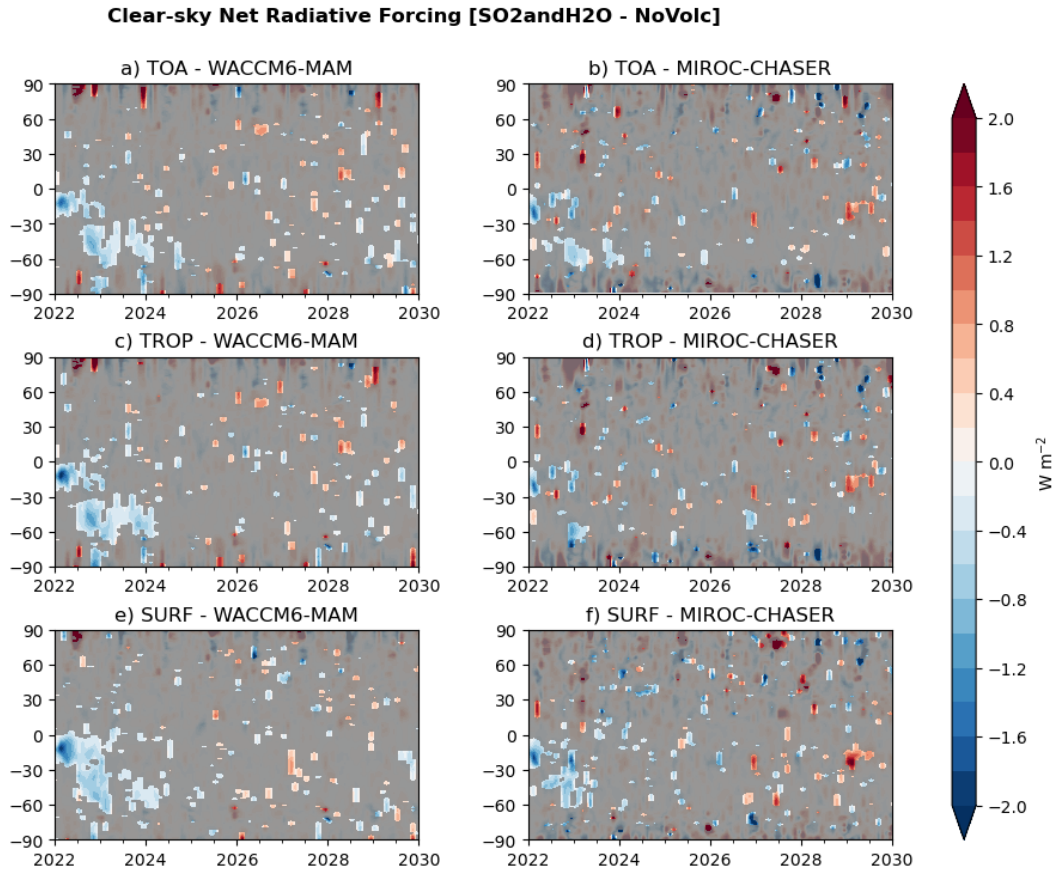


**Figure A6.** Time series of zonal mean radiative forcing under clear-sky conditions for the SO<sub>2</sub>andH<sub>2</sub>O experiment with fixed SST (Fixed-SST). RF is calculated at TOA (a and b), TROP (b and c), and SURF (e and f) in WACCM6-MAM (first column) and MIROC-CHASER (second column). Gray areas indicate regions where the differences are not statistically significant at the 5% level based on Student's t-test.

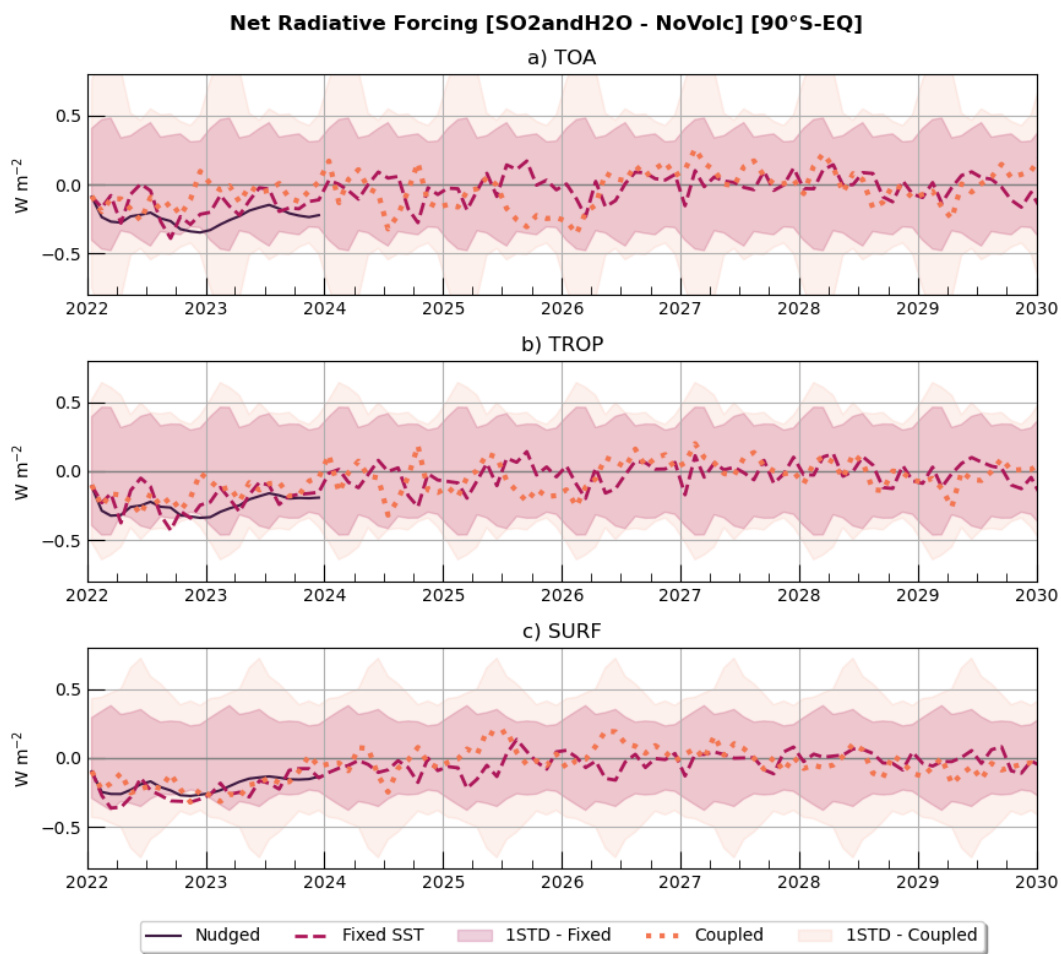


**Figure A7.** Time series of global net radiative forcing under clear-sky conditions for SO<sub>2</sub>andH<sub>2</sub>O experiment in WACCM6-MAM at TOA (a), TROP (b), and SURF (c). Solid lines indicate the results from nudged simulation (Nudged), dashed lines from the fixed SST simulation (Fixed-SST) and dotted lines from the coupled experiment (Coupled). Shading indicates the monthly internal variability, calculated as 1 standard deviation over 10-year simulations using a 30-member ensemble from the unperturbed NoVolc experiment.

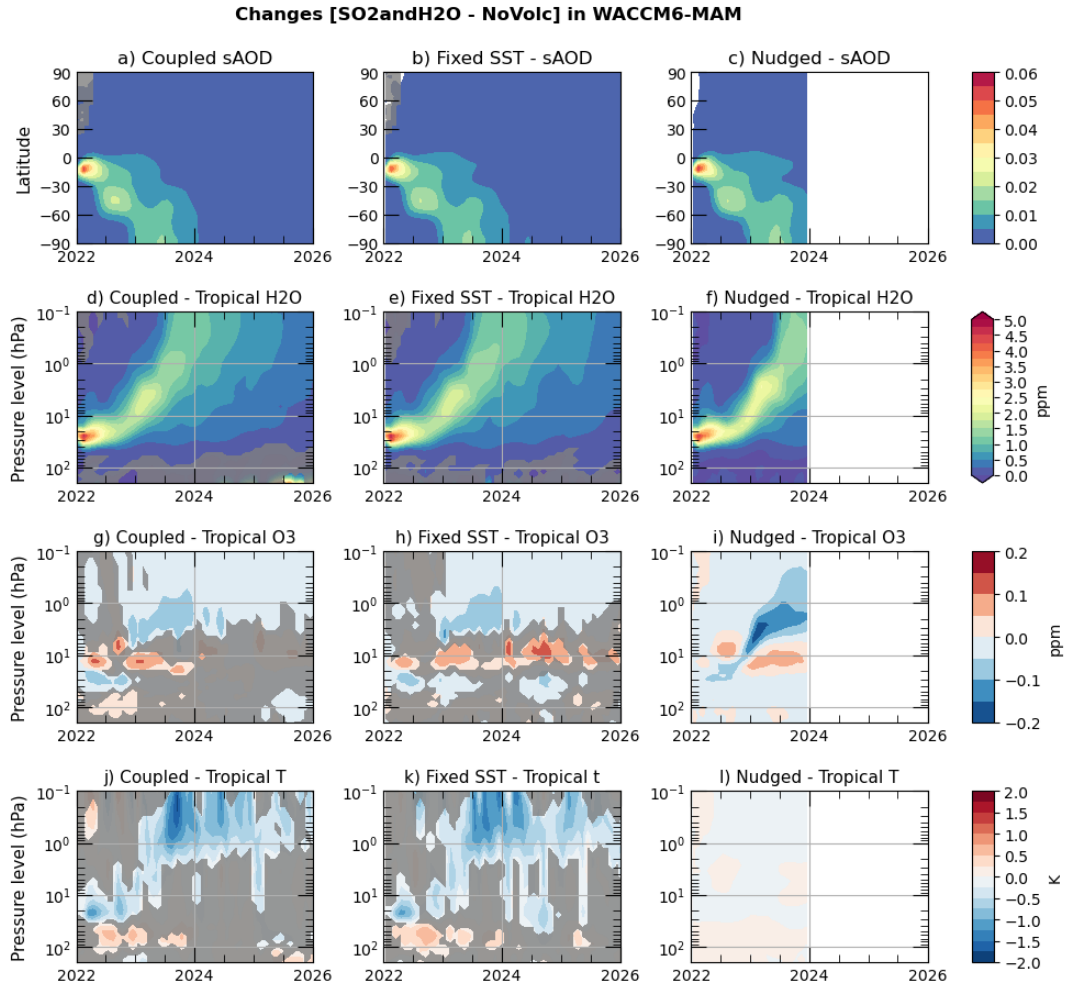


**Figure A8.** Time series of zonal mean ~~gas-radiation interaction RF under clear-sky conditions for the SO<sub>2</sub>andH<sub>2</sub>O experiment~~ changes in stratospheric aerosol optical depth (sAOD; panels a–c), at TOA tropical stratospheric H<sub>2</sub>O concentrations (a–e 30°S–30°N; panels d–f, in ppm), tropical stratospheric O<sub>3</sub> concentrations (30°S–30°N; panels g–i, in ppm), and SURF tropical stratospheric temperature (d–f 30°S–30°N; panels j–l, in K). Each column represents a different model setup: first and second columns Changes are free-running experiments with either coupled ocean or climatological sea surface temperatures computed as the difference between the SO<sub>2</sub>andH<sub>2</sub>O and sea ice NoVolc experiments for the (Coupled and Fixed-SST<sub>a</sub>, respectively d, g, j) Coupled, third column indicates nudged simulations (Nudged<sub>b, e, h, k</sub>) –Results from Fixed-SST<sub>a</sub> and Coupled are ensemble means (c, f, i, l) Nudged configurations. Gray areas indicate regions where the differences are not statistically significant at the 5% level based on Student’s t-test.

Time series of global-net radiative forcing under clear-sky conditions for SO<sub>2</sub> and H<sub>2</sub>O experiment in WACCM6-MAM at TOA (a), TROP (b), and SURF (c). Solid lines indicate the results from nudged simulation (Nudged), dashed lines from the fixed SST simulation (Fixed-SST) and dotted lines from the coupled experiment (Coupled). Shading indicates the monthly internal variability, calculated as  $\pm 1$  standard deviation over 10-year simulations using a 30-member ensemble from the unperturbed NoVole experiment.

Time series of global-net radiative forcing under clear-sky conditions for SO<sub>2</sub> and H<sub>2</sub>O experiment in WACCM6-MAM at TOA (a), TROP (b), and SURF (c). Solid lines indicate the results from nudged simulation (Nudged), dashed lines from the fixed SST simulation (Fixed-SST) and dotted lines from the coupled experiment (Coupled). Shading indicates the monthly internal variability, calculated as  $\pm 1$  standard deviation over 10-year simulations using a 30-member ensemble from the unperturbed NoVole experiment.

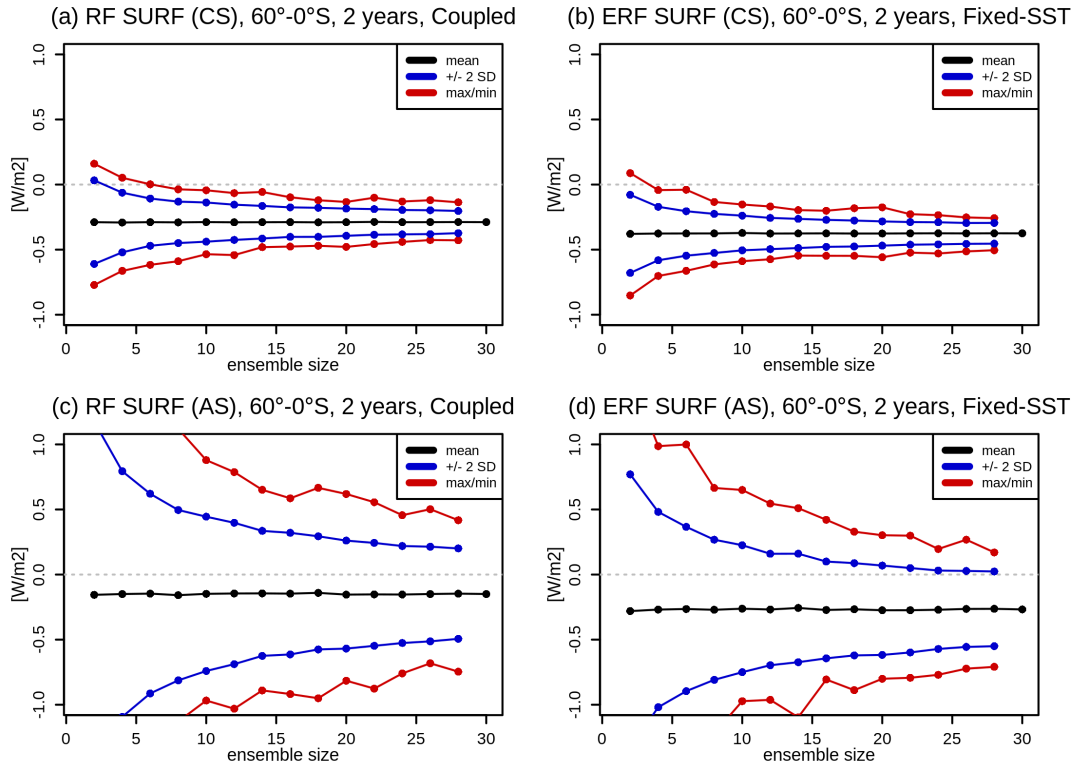


**Figure A9.** Detectability of the 2022-2023 average RF SURF response in the Coupled simulations (left) and the ERF response in the Fixed-SST simulations (right) for clear-sky (top) and all-sky (bottom) conditions. Results obtained by randomly subsampling each ensemble with replacement to obtain 2000 artificial ensembles each of different ensemble size. Black lines denote the mean response, and blue and red lines indicate the  $\pm 2$  standard deviation and the max/min ranges, respectively, of the possible responses. The results show that a 2-year mean clear-sky RF/ERF response is detectable already with a few ensemble members ( $\sim 5$ ) but requires more members to constrain the magnitude with any confidence. In contrast, the uncertainty of the all-sky response is substantially larger, particularly in the Coupled experiment but also in the Fixed-SST experiment, where even 30 ensemble members may be insufficient to determine even the sign of the response with any confidence.

**Table A1.** Global effective radiative forcing (in  $\text{W m}^{-2}$ ) at the Top of Atmosphere under clear-sky conditions.

Model	6 Months	1 Year	2 Years	5 Years	10 Years
WACCM6-MAM	$-0.11 \pm 0.15$	$-0.18 \pm 0.13$	$-0.16 \pm 0.09$	$-0.07 \pm 0.07$	$-0.03 \pm 0.06$
MIROC-CHASER	$-0.08 \pm 0.17$	$-0.15 \pm 0.12$	$-0.11 \pm 0.10$	$-0.10 \pm 0.08$	$-0.04 \pm 0.06$

480 ~~Time series of net, shortwave (SW), and longwave (LW) gas-radiation interaction RF (sAOD; panels a–c), tropical H<sub>2</sub>O concentrations and tropical temperature at 10 hPa (30S–30N; panels d–f, in ppm and K, respectively), and tropical O<sub>3</sub> concentrations and tropical temperature at 70 hPa (30S–30N; panels g–i, in ppm and K, respectively). Changes are computed as the difference between the SO<sub>2</sub> and H<sub>2</sub>O and NoVolc experiments for the (a, d, g) Coupled, (b, e, h) Fixed-SST, and (c, f, i) Nudged configurations.~~

**Table A2.** Effective radiative forcing (in  $\text{W m}^{-2}$ ) at the Tropopause under clear-sky conditions. Forcing is averaged between 60°S and the equator.

Model	6 Months	1 Year	2 Years	5 Years	10 Years
WACCM6-MAM	$-0.40 \pm 0.14$	$-0.44 \pm 0.15$	$-0.34 \pm 0.11$	$-0.15 \pm 0.06$	$-0.09 \pm 0.05$
MIROC-CHASER	$-0.25 \pm 0.15$	$-0.31 \pm 0.12$	$-0.21 \pm 0.12$	$-0.12 \pm 0.03$	$-0.04 \pm 0.05$

**Table A3.** Effective radiative forcing (in  $\text{W m}^{-2}$ ) at the Surface under clear-sky conditions. Forcing is averaged between 60°S and the equator.

Model	6 Months	1 Year	2 Years	5 Years	10 Years
WACCM6-MAM	$-0.53 \pm 0.16$	$-0.51 \pm 0.16$	$-0.37 \pm 0.10$	$-0.18 \pm 0.07$	$-0.09 \pm 0.07$
MIROC-CHASER	$-0.42 \pm 0.12$	$-0.48 \pm 0.09$	$-0.33 \pm 0.08$	$-0.19 \pm 0.06$	$-0.08 \pm 0.03$

*Data availability.* The HTHH–MOC model simulation data are available on JASMIN, the collaborative data analysis environment of UK  
485 (<https://www.jasmin.ac.uk>, last access: 5 December 2025).

*Author contributions.* IQ performed all analyses and wrote the manuscript with DV and EB. XW, EB, JZ, WY, and ZZ performed the WACCM6-MAM simulations. YZ designed the simulations. GS assisted with the analyses and contributed to the discussion of the results. C-CL performed the WACCM6-CARMA simulations with ST. GM performed the UKESM simulations. YP and PY performed the CAM5-CARMA simulations. SW conducted MIROC-CHASER simulations, postprocessed and uploaded the model data on JASMIN, under  
490 supervision of TS, who developed the model aerosol microphysics scheme. All authors contributed to the revision of the manuscript.

*Competing interests.* The authors declare no competing interest. Some authors are editorial board members of the journal ACP.

*Acknowledgements.* NCAR’s Community Earth System Model project is supported primarily by the National Science Foundation under Cooperative Agreement No. 1852977. Computing and data storage resources, including the Derecho supercomputer (doi:10.5065/qx9a-pg09), were provided by the Computational and Information Systems Laboratory (CISL) at NCAR. Ilaria Quaglia acknowledges support from the  
495 US Simons Foundation (grant ref. MPS-SRM-00005203). Ewa Bednarz acknowledges support from the National Oceanic and Atmospheric Administration (NOAA) cooperative agreement NA22OAR4320151 and the Earth’s Radiative Budget (ERB) program. Simone Tilmes acknowledges support by the NOAA Climate Program Office Earth’s Radiation Budget award no. 03-01-07-001 and NA22OAR4310477. Shingo Watanabe and Takashi Sekiya were supported by MEXT-Program for the advanced studies of climate change projection (SENTAN) Grant Number JPMXD0722681344. MIROC-CHASER simulations were performed using the Earth Simulator. [Wandi Yu’s work is prepared by LLNL under Contract DE-AC52-07NA27344.](https://futureoflife.org/) [Zhihong Zhuo is supported by the Future of Life Institute \(https://futureoflife.org/\), project title “Constraining Nuclear War Fire Emissions and their Impacts on the Climate System.](https://futureoflife.org/)  
500

## References

- Andersson, S. M., Martinsson, B. G., Vernier, J.-P., Friberg, J., Brenninkmeijer, C. A. M., Hermann, M., van Velthoven, P. F. J., and Zahn, A.: Significant radiative impact of volcanic aerosol in the lowermost stratosphere, *Nature Communications*, 6, 7692, <https://doi.org/10.1038/ncomms8692>, 2015.
- 505 Baran, A. J. and Foot, J. S.: New application of the operational sounder HIRS in determining a climatology of sulphuric acid aerosol from the Pinatubo eruption, *Journal of Geophysical Research*, 99, 25 673, <https://doi.org/10.1029/94JD02044>, 1994.
- Bednarz, E. M., Butler, A. H., Wang, X., Zhuo, Z., Yu, W., Stenchikov, G., Toohey, M., and Zhu, Y.: Indirect climate impacts of the Hunga eruption, *EGU sphere*, 2025, 1–30, <https://doi.org/10.5194/egusphere-2025-1970>, 2025.
- 510 Brodowsky, C., Sukhodolov, T., Feinberg, A., Höpfner, M., Peter, T., Stenke, A., and Rozanov, E.: Modeling the Sulfate Aerosol Evolution After Recent Moderate Volcanic Activity, 2008–2012, *Journal of Geophysical Research: Atmospheres*, 126, e2021JD035 472, <https://doi.org/https://doi.org/10.1029/2021JD035472>, e2021JD035472 2021JD035472, 2021.
- Brodowsky, C. V., Sukhodolov, T., Chiodo, G., Aquila, V., Bekki, S., Dhomse, S. S., Höpfner, M., Laakso, A., Mann, G. W., Niemeier, U., Pitari, G., Quaglia, I., Rozanov, E., Schmidt, A., Sekiya, T., Tilmes, S., Timmreck, C., Vattioni, S., Vioni, D., Yu, P., Zhu, Y., and Peter, 515 T.: Analysis of the global atmospheric background sulfur budget in a multi-model framework, *Atmospheric Chemistry and Physics*, 24, 5513–5548, <https://doi.org/10.5194/acp-24-5513-2024>, 2024.
- Carn, S. A., Fioletov, V. E., McLinden, C. A., Li, C., and Krotkov, N. A.: A decade of global volcanic SO<sub>2</sub> emissions measured from space, *Scientific Reports*, 7, 44 095, <https://doi.org/10.1038/srep44095>, 2017.
- Carn, S. A., Krotkov, N. A., Fisher, B. L., and Li, C.: Out of the blue: Volcanic SO<sub>2</sub> emissions during the 2021–2022 eruptions of Hunga 520 Tonga–Hunga Ha’apai (Tonga), *Frontiers in Earth Science*, Volume 10 - 2022, <https://doi.org/10.3389/feart.2022.976962>, 2022.
- Carr, J. L., Horváth, , Wu, D. L., and Friberg, M. D.: Stereo Plume Height and Motion Retrievals for the Record-Setting Hunga Tonga-Hunga Ha’apai Eruption of 15 January 2022, *Geophysical Research Letters*, 49, e2022GL098 131, <https://doi.org/https://doi.org/10.1029/2022GL098131>, e2022GL098131 2022GL098131, 2022.
- Cattiaux, J., Ribes, A., and Cariou, E.: How Extreme Were Daily Global Temperatures in 2023 and Early 2024?, *Geophysical Research 525 Letters*, 51, e2024GL110 531, <https://doi.org/https://doi.org/10.1029/2024GL110531>, e2024GL110531 2024GL110531, 2024.
- Chrysanthou, A., Maycock, A. C., Chipperfield, M. P., Dhomse, S., Garny, H., Kinnison, D., Akiyoshi, H., Deushi, M., Garcia, R. R., Jöckel, P., Kirner, O., Pitari, G., Plummer, D. A., Revell, L., Rozanov, E., Stenke, A., Tanaka, T. Y., Vioni, D., and Yamashita, Y.: The effect of atmospheric nudging on the stratospheric residual circulation in chemistry–climate models, *Atmospheric Chemistry and Physics*, 19, 11 559–11 586, <https://doi.org/10.5194/acp-19-11559-2019>, 2019.
- 530 Chung, E.-S. and Soden, B. J.: An Assessment of Direct Radiative Forcing, Radiative Adjustments, and Radiative Feedbacks in Coupled Ocean–Atmosphere Models, *Journal of Climate*, 28, 4152 – 4170, <https://doi.org/10.1175/JCLI-D-14-00436.1>, 2015.
- Davis, N. A., Vioni, D., Garcia, R. R., Kinnison, D. E., Marsh, D. R., Mills, M., Richter, J. H., Tilmes, S., Bardeen, C. G., Gettelman, A., Glanville, A. A., MacMartin, D. G., Smith, A. K., and Vitt, F.: Climate, Variability, and Climate Sensitivity of “Middle Atmosphere” Chemistry Configurations of the Community Earth System Model Version 2, Whole Atmosphere Community Climate Model Version 6 (CESM2(WACCM6)), *Journal of Advances in Modeling Earth Systems*, 15, e2022MS003 579, <https://doi.org/https://doi.org/10.1029/2022MS003579>, e2022MS003579 2022MS003579, 2023.
- 535

- Davis, S. M., Rosenlof, K. H., Hassler, B., Hurst, D. F., Read, W. G., Vömel, H., Selkirk, H., Fujiwara, M., and Damadeo, R.: The Stratospheric Water and Ozone Satellite Homogenized (SWOOSH) database: a long-term database for climate studies, *Earth System Science Data*, 8, 461–490, <https://doi.org/10.5194/essd-8-461-2016>, 2016.
- 540 Fisher, B. L., Krotkov, N. A., Bhartia, P. K., Li, C., Carn, S. A., Hughes, E., and Leonard, P. J. T.: A new discrete wavelength backscattered ultraviolet algorithm for consistent volcanic SO<sub>2</sub> retrievals from multiple satellite missions, *Atmospheric Measurement Techniques*, 12, 5137–5153, <https://doi.org/10.5194/amt-12-5137-2019>, 2019.
- Fleming, E. L., Newman, P. A., Liang, Q., and Oman, L. D.: Stratospheric Temperature and Ozone Impacts of the Hunga Tonga-Hunga Ha’apai Water Vapor Injection, *Journal of Geophysical Research: Atmospheres*, 129, e2023JD039298, <https://doi.org/https://doi.org/10.1029/2023JD039298>, e2023JD039298 2023JD039298, 2024.
- 545 Forster, P. M., Richardson, T., Maycock, A. C., Smith, C. J., Samset, B. H., Myhre, G., Andrews, T., Pincus, R., and Schulz, M.: Recommendations for diagnosing effective radiative forcing from climate models for CMIP6, *Journal of Geophysical Research: Atmospheres*, 121, 12,460–12,475, <https://doi.org/https://doi.org/10.1002/2016JD025320>, 2016.
- Forster, P. M., Smith, C. J., Walsh, T., Lamb, W. F., Lamboll, R., Hauser, M., Ribes, A., Rosen, D., Gillett, N., Palmer, M. D., Rogelj, J., von Schuckmann, K., Seneviratne, S. I., Trewin, B., Zhang, X., Allen, M., Andrew, R., Birt, A., Borger, A., Boyer, T., Broersma, J. A., Cheng, L., Dentener, F., Friedlingstein, P., GutiÃ©rrez, J. M., GÃ¼ttschow, J., Hall, B., Ishii, M., Jenkins, S., Lan, X., Lee, J.-Y., Morice, C., Kadow, C., Kennedy, J., Killick, R., Minx, J. C., Naik, V., Peters, G. P., Pirani, A., Pongratz, J., Schleussner, C.-F., Szopa, S., Thorne, P., Rohde, R., Rojas Corradi, M., Schumacher, D., Vose, R., Zickfeld, K., Masson-Delmotte, V., and Zhai, P.: Indicators of Global Climate Change 2022: annual update of large-scale indicators of the state of the climate system and human influence, *Earth System Science Data*, 15, 2295–2327, <https://doi.org/10.5194/essd-15-2295-2023>, 2023.
- 555 Forster, P. M., Smith, C., Walsh, T., Lamb, W. F., Lamboll, R., Cassou, C., Hauser, M., Hausfather, Z., Lee, J.-Y., Palmer, M. D., von Schuckmann, K., Slangen, A. B. A., Szopa, S., Trewin, B., Yun, J., Gillett, N. P., Jenkins, S., Matthews, H. D., Raghavan, K., Ribes, A., Rogelj, J., Rosen, D., Zhang, X., Allen, M., Aleluia Reis, L., Andrew, R. M., Betts, R. A., Borger, A., Broersma, J. A., Burgess, S. N., Cheng, L., Friedlingstein, P., Domingues, C. M., Gambarini, M., Gasser, T., GÃ¼tschow, J., Ishii, M., Kadow, C., Kennedy, J., Killick, R. E., Krummel, P. B., Liné, A., Monselesan, D. P., Morice, C., Mühle, J., Naik, V., Peters, G. P., Pirani, A., Pongratz, J., Minx, J. C., Rigby, M., Rohde, R., Savita, A., Seneviratne, S. I., Thorne, P., Wells, C., Western, L. M., van der Werf, G. R., Wijkffels, S. E., Masson-Delmotte, V., and Zhai, P.: Indicators of Global Climate Change 2024: annual update of key indicators of the state of the climate system and human influence, *Earth System Science Data*, 17, 2641–2680, <https://doi.org/10.5194/essd-17-2641-2025>, 2025.
- 560 Gettelman, A., Mills, M., Kinnison, D., Garcia, R., Smith, A., Marsh, D., Tilmes, S., Vitt, F., Bardeen, C., Mcinerney, J., Liu, H., Solomon, S., Polvani, L., Emmons, L., Lamarque, J.-F., Richter, J., Glanville, A., Bacmeister, J., Phillips, A., and Randel, W.: The Whole Atmosphere Community Climate Model Version 6 (WACCM6), *Journal of Geophysical Research: Atmospheres*, 124, <https://doi.org/10.1029/2019JD030943>, 2019.
- Jenkins, S., Smith, C., Allen, M., and Grainger, R.: Tonga eruption increases chance of temporary surface temperature anomaly above 1.5âˆ°C, *Nature Climate Change*, 13, 127–129, <https://doi.org/10.1038/s41558-022-01568-2>, 2023.
- 570 Kloss, C., Berthet, G., Sellitto, P., Ploeger, F., Taha, G., Tidiga, M., Eremenko, M., Bossolasco, A., Jégou, F., Renard, J.-B., and Legras, B.: Stratospheric aerosol layer perturbation caused by the 2019 Raikoke and Ulawun eruptions and their radiative forcing, *Atmospheric Chemistry and Physics*, 21, 535–560, <https://doi.org/10.5194/acp-21-535-2021>, 2021.
- Kovilakam, M., Thomason, L. W., Ernest, N., Rieger, L., Bourassa, A., and Millán, L.: The Global Space-based Stratospheric Aerosol Climatology (version 2.0): 1979–2018, *Earth System Science Data*, 12, 2607–2634, <https://doi.org/10.5194/essd-12-2607-2020>, 2020.

- 575 Kovilakam, M., Thomason, L. W., Verkerk, M., Aubry, T., and Knepp, T. N.: OMPS-LP aerosol extinction coefficients and their applicability in GloSSAC, *Atmospheric Chemistry and Physics*, 25, 535–553, <https://doi.org/10.5194/acp-25-535-2025>, 2025.
- Kremser, S., Thomason, L. W., von Hobe, M., Hermann, M., Deshler, T., Timmreck, C., Toohey, M., Stenke, A., Schwarz, J. P., Weigel, R., Fueglistaler, S., Prata, F. J., Vernier, J.-P., Schlager, H., Barnes, J. E., Antuña-Marrero, J.-C., Fairlie, D., Palm, M., Mahieu, E., Notholt, J., Rex, M., Bingen, C., Vanhellemont, F., Bourassa, A., Plane, J. M. C., Klocke, D., Carn, S. A., Clarisse, L., Trickl, T., Neely, R., James, 580 A. D., Rieger, L., Wilson, J. C., and Meland, B.: Stratospheric aerosol-Observations, processes, and impact on climate: Stratospheric Aerosol, *Reviews of Geophysics*, 54, 278–335, <https://doi.org/10.1002/2015RG000511>, 2016.
- Kroll, C. A. and Schmidt, A.: Indirect stratospheric moisture increase after a Pinatubo-magnitude eruption can be comparable to direct increase after 2022 Hunga, *Communications Earth & Environment*, 5, 497, <https://doi.org/10.1038/s43247-024-01651-w>, 2024.
- Lamarque, J.-F., Emmons, L. K., Hess, P. G., Kinnison, D. E., Tilmes, S., Vitt, F., Heald, C. L., Holland, E. A., Lauritzen, P. H., Neu, 585 J., Orlando, J. J., Rasch, P. J., and Tyndall, G. K.: CAM-chem: description and evaluation of interactive atmospheric chemistry in the Community Earth System Model, *Geoscientific Model Development*, 5, 369–411, <https://doi.org/10.5194/gmd-5-369-2012>, 2012.
- Li, C., Peng, Y., Asher, E., Baron, A. A., Todt, M., Thornberry, T. D., Evan, S., Brioude, J., Smale, P., Querel, R., Rosenlof, K. H., Zhou, L., Xu, J., Qie, K., Bian, J., Toon, O. B., Zhu, Y., and Yu, P.: Microphysical Simulation of the 2022 Hunga Volcano Eruption Using a Sectional Aerosol Model, *Geophysical Research Letters*, 51, e2024GL108 522, <https://doi.org/https://doi.org/10.1029/2024GL108522>, 590 e2024GL108522 2024GL108522, 2024.
- Li, Y., Pedersen, C., Dykema, J., Vernier, J.-P., Vattioni, S., Pandit, A. K., Stenke, A., Asher, E., Thornberry, T., Todt, M. A., Bui, T. P., Dean-Day, J., and Keutsch, F. N.: In situ measurements of perturbations to stratospheric aerosol and modeled ozone and radiative impacts following the 2021 La Soufrière eruption, *Atmospheric Chemistry and Physics*, 23, 15 351–15 364, <https://doi.org/10.5194/acp-23-15351-2023>, 2023.
- 595 Liu, X., Easter, R. C., Ghan, S. J., Zaveri, R., Rasch, P., Shi, X., Lamarque, J.-F., Gettelman, A., Morrison, H., Vitt, F., Conley, A., Park, S., Neale, R., Hannay, C., Ekman, A. M. L., Hess, P., Mahowald, N., Collins, W., Iacono, M. J., Bretherton, C. S., Flanner, M. G., and Mitchell, D.: Toward a minimal representation of aerosols in climate models: description and evaluation in the Community Atmosphere Model CAM5, *Geoscientific Model Development*, 5, 709–739, <https://doi.org/10.5194/gmd-5-709-2012>, 2012.
- Liu, X., Ma, P.-L., Wang, H., Tilmes, S., Singh, B., Easter, R. C., Ghan, S. J., and Rasch, P. J.: Description and evaluation of a new four- 600 mode version of the Modal Aerosol Module (MAM4) within version 5.3 of the Community Atmosphere Model, *Geoscientific Model Development*, 9, 505–522, <https://doi.org/10.5194/gmd-9-505-2016>, 2016.
- Mills, M. J., Schmidt, A., Easter, R., Solomon, S., Kinnison, D. E., Ghan, S. J., Neely III, R. R., Marsh, D. R., Conley, A., Bardeen, C. G., and Gettelman, A.: Global volcanic aerosol properties derived from emissions, 1990–2014, using CESM1(WACCM), *Journal of Geophysical Research: Atmospheres*, 121, 2332–2348, <https://doi.org/https://doi.org/10.1002/2015JD024290>, 2016.
- 605 Millán, L., Santee, M. L., Lambert, A., Livesey, N. J., Werner, F., Schwartz, M. J., Pumphrey, H. C., Manney, G. L., Wang, Y., Su, H., Wu, L., Read, W. G., and Froidevaux, L.: The Hunga Tonga-Hunga Ha’apai Hydration of the Stratosphere, *Geophysical Research Letters*, 49, e2022GL099 381, <https://doi.org/https://doi.org/10.1029/2022GL099381>, e2022GL099381 2022GL099381, 2022.
- Mulcahy, J. P., Jones, C. G., Rumbold, S. T., Kuhlbrodt, T., Dittus, A. J., Blockley, E. W., Yool, A., Walton, J., Hardacre, C., Andrews, T., Bodas-Salcedo, A., Stringer, M., de Mora, L., Harris, P., Hill, R., Kelley, D., Robertson, E., and Tang, Y.: UKESM1.1: develop- 610 ment and evaluation of an updated configuration of the UK Earth System Model, *Geoscientific Model Development*, 16, 1569–1600, <https://doi.org/10.5194/gmd-16-1569-2023>, 2023.

- Myhre, G., Shindell, D., Bréon, F.-M., Collins, W., Fuglestedt, J., Huang, J., Koch, D., Lamarque, J.-F., Lee, D., Mendoza, B., Nakajima, T., Robock, A., Stephens, G., Takemura, T., and Zhang, H.: Anthropogenic and natural radiative forcing, pp. 659–740, Cambridge University Press, Cambridge, UK, <https://doi.org/10.1017/CBO9781107415324.018>, 2013.
- 615 NASA/LARC/SD/ASDC: Global Space-based Stratospheric Aerosol Climatology Version 2.22, <https://doi.org/10.5067/GLOSSAC-L3-V2.22>.
- Quaglia, I. and Visioni, D.: Modeling 2020 regulatory changes in international shipping emissions helps explain anomalous 2023 warming, *Earth System Dynamics*, 15, 1527–1541, <https://doi.org/10.5194/esd-15-1527-2024>, 2024.
- Quaglia, I., Timmreck, C., Niemeier, U., Visioni, D., Pitari, G., Brodowsky, C., Brühl, C., Dhomse, S. S., Franke, H., Laakso, A., Mann, 620 G. W., Rozanov, E., and Sukhodolov, T.: Interactive stratospheric aerosol models' response to different amounts and altitudes of SO<sub>2</sub> injection during the 1991 Pinatubo eruption, *Atmospheric Chemistry and Physics*, 23, 921–948, <https://doi.org/10.5194/acp-23-921-2023>, 2023.
- Ramaswamy, V., Collins, W., Haywood, J., Lean, J., Mahowald, N., Myhre, G., Naik, V., Shine, K. P., Soden, B., Stenchikov, G., and Storelvmo, T.: Radiative Forcing of Climate: The Historical Evolution of the Radiative Forcing Concept, the Forcing Agents and their 625 Quantification, and Applications, *Meteorological Monographs*, 59, 14.1 – 14.101, <https://doi.org/10.1175/AMSMONOGRAPHS-D-19-0001.1>, 2018.
- Randel, W. J., Garcia, R. R., Calvo, N., and Marsh, D.: ENSO influence on zonal mean temperature and ozone in the tropical lower stratosphere, *Geophysical Research Letters*, 36, <https://doi.org/https://doi.org/10.1029/2009GL039343>, 2009.
- Randel, W. J., Wang, X., Starr, J., Garcia, R. R., and Kinnison, D.: Long-Term Temperature Impacts of the Hunga Volcanic Eruption in 630 the Stratosphere and Above, *Geophysical Research Letters*, 51, e2024GL111500, <https://doi.org/https://doi.org/10.1029/2024GL111500>, e2024GL111500 2024GL111500, 2024.
- Schmidt, A., Mills, M. J., Ghan, S., Gregory, J. M., Allan, R. P., Andrews, T., Bardeen, C. G., Conley, A., Forster, P. M., Gettelman, A., Portmann, R. W., Solomon, S., and Toon, O. B.: Volcanic Radiative Forcing From 1979 to 2015, *Journal of Geophysical Research: Atmospheres*, 123, 12 491–12 508, <https://doi.org/https://doi.org/10.1029/2018JD028776>, 2018.
- 635 Schoeberl, M. R., Wang, Y., Taha, G., Zawada, D. J., Ueyama, R., and Dessler, A.: Evolution of the Climate Forcing During the Two Years After the Hunga Tonga-Hunga Ha'apai Eruption, *Journal of Geophysical Research: Atmospheres*, 129, e2024JD041296, <https://doi.org/https://doi.org/10.1029/2024JD041296>, e2024JD041296 2024JD041296, 2024.
- Sekiya, T., Sudo, K., and Nagai, T.: Evolution of stratospheric sulfate aerosol from the 1991 Pinatubo eruption: Roles of aerosol microphysical processes, *Journal of Geophysical Research: Atmospheres*, 121, 2911–2938, <https://doi.org/https://doi.org/10.1002/2015JD024313>, 2016.
- 640 Sellitto, P., Podglajen, A., Belhadji, R., Boichu, M., Carboni, E., Cuesta, J., Duchamp, C., Kloss, C., Siddans, R., BÃšgue, N., Blarel, L., Jegou, F., Khaykin, S., Renard, J. B., and Legras, B.: The unexpected radiative impact of the Hunga Tonga eruption of 15th January 2022, *Communications Earth & Environment*, 3, 288, <https://doi.org/10.1038/s43247-022-00618-z>, 2022.
- Sellitto, P., Siddans, R., Belhadji, R., Carboni, E., Legras, B., Podglajen, A., Duchamp, C., and Kerridge, B.: Observing the SO<sub>2</sub> and Sulfate Aerosol Plumes From the 2022 Hunga Eruption With the Infrared Atmospheric Sounding Interferometer (IASI), *Geophysical Research 645 Letters*, 51, e2023GL105565, <https://doi.org/https://doi.org/10.1029/2023GL105565>, e2023GL105565 2023GL105565, 2024.
- Sellitto, P., Belhadji, R., Legras, B., Podglajen, A., and Duchamp, C.: The optical properties of the stratospheric aerosol layer perturbation of the Hunga Tonga–Hunga Ha'apai volcano eruption of 15 January 2022, *Atmospheric Chemistry and Physics*, 25, 6353–6364, <https://doi.org/10.5194/acp-25-6353-2025>, 2025.

- Sherwood, S. C., Bony, S., Boucher, O., Bretherton, C., Forster, P. M., Gregory, J. M., and Stevens, B.: Adjustments in the Forcing-Feedback Framework for Understanding Climate Change, *Bulletin of the American Meteorological Society*, 96, 217 – 228, <https://doi.org/10.1175/BAMS-D-13-00167.1>, 2015.
- Smith, C. J., Kramer, R. J., Myhre, G., Forster, P. M., Soden, B. J., Andrews, T., Boucher, O., Faluvegi, G., Fläschner, D., Hodnebrog, K., Kasoar, M., Kharin, V., Kirkevåg, A., Lamarque, J.-F., Mülmenstädt, J., Olivie, D., Richardson, T., Samset, B. H., Shindell, D., Stier, P., Takemura, T., Voulgarakis, A., and Watson-Parris, D.: Understanding Rapid Adjustments to Diverse Forcing Agents, *Geophysical Research Letters*, 45, 12,023–12,031, <https://doi.org/10.1029/2018GL079826>, 2018.
- Solomon, S., Rosenlof, K. H., Portmann, R. W., Daniel, J. S., Davis, S. M., Sanford, T. J., and Plattner, G.-K.: Contributions of stratospheric water vapor to decadal changes in the rate of global warming, *Science*, 327, 1219–1223, 2010.
- Staunton-Sykes, J., Aubry, T. J., Shin, Y. M., Weber, J., Marshall, L. R., Luke Abraham, N., Archibald, A., and Schmidt, A.: Co-emission of volcanic sulfur and halogens amplifies volcanic effective radiative forcing, *Atmospheric Chemistry and Physics*, 21, 9009–9029, <https://doi.org/10.5194/acp-21-9009-2021>, 2021.
- Stenchikov, G., Ukhov, A., and Osipov, S.: Modeling the Radiative Forcing and Atmospheric Temperature Perturbations Caused by the 2022 Hunga Volcano Explosion, *Journal of Geophysical Research: Atmospheres*, 130, e2024JD041940, <https://doi.org/10.1029/2024JD041940>, e2024JD041940 2024JD041940, 2025.
- Stenchikov, G. L., Kirchner, I., Robock, A., Graf, H.-F., Antuña, J. C., Grainger, R. G., Lambert, A., and Thomason, L.: Radiative forcing from the 1991 Mount Pinatubo volcanic eruption, *Journal of Geophysical Research: Atmospheres*, 103, 13 837–13 857, <https://doi.org/10.1029/98JD00693>, 1998.
- Thomason, L. W., Ernest, N., Millán, L., Rieger, L., Bourassa, A., Vernier, J.-P., Manney, G., Luo, B., Arfeuille, F., and Peter, T.: A global space-based stratospheric aerosol climatology: 1979–2016, *Earth System Science Data*, 10, 469–492, <https://doi.org/10.5194/essd-10-469-2018>, 2018.
- Tilmes, S., Mills, M. J., Zhu, Y., Bardeen, C. G., Vitt, F., Yu, P., Fillmore, D., Liu, X., Toon, B., and Deshler, T.: Description and performance of a sectional aerosol microphysical model in the Community Earth System Model (CESM2), *Geoscientific Model Development*, 16, 6087–6125, <https://doi.org/10.5194/gmd-16-6087-2023>, 2023.
- Ukhov, A., Stenchikov, G., Osipov, S., Krotkov, N., Gorkavii, N., Li, C., Dubovik, O., and Lopatin, A.: Inverse Modeling of the Initial Stage of the 1991 Pinatubo Volcanic Cloud Accounting for Radiative Feedback of Volcanic Ash, *Journal of Geophysical Research: Atmospheres*, 128, e2022JD038446, <https://doi.org/10.1029/2022JD038446>, e2022JD038446 2022JD038446, 2023.
- Wrana, F., Niemeier, U., Thomason, L. W., Wallis, S., and von Savigny, C.: Stratospheric aerosol size reduction after volcanic eruptions, *Atmospheric Chemistry and Physics*, 23, 9725–9743, <https://doi.org/10.5194/acp-23-9725-2023>, 2023.
- Yu, P., Toon, O. B., Bardeen, C. G., Mills, M. J., Fan, T., English, J. M., and Neely, R. R.: Evaluations of tropospheric aerosol properties simulated by the community earth system model with a sectional aerosol microphysics scheme, *Journal of Advances in Modeling Earth Systems*, 7, 865–914, <https://doi.org/10.1002/2014MS000421>, 2015.
- Zhu, Y., Toon, O. B., Jensen, E. J., Bardeen, C. G., Mills, M. J., Tolbert, M. A., Yu, P., and Woods, S.: Persisting volcanic ash particles impact stratospheric SO<sub>2</sub> lifetime and aerosol optical properties, *Nature Communications*, 11, <https://doi.org/10.1038/s41467-020-18352-5>, 2020.
- Zhu, Y., Bardeen, C. G., Tilmes, S., Mills, M. J., Wang, X., Harvey, V. L., Taha, G., Kinnison, D., Portmann, R. W., Yu, P., Rosenlof, K. H., Avery, M., Kloss, C., Li, C., Glanville, A. S., Millán, L., Deshler, T., Krotkov, N., and Toon, O. B.: Perturbations in stratospheric aerosol evolution due to the water-rich plume of the 2022 Hunga-Tonga eruption, *Communications Earth & Environment*, 3, 248, <https://doi.org/10.1038/s43247-022-00580-w>, 2022.

- Zhu, Y., Akiyoshi, H., Aquila, V., Asher, E., Bednarz, E. M., Bekki, S., Brühl, C., Butler, A. H., Case, P., Chabrillat, S., Chiodo, G., Clyne, M., Colarco, P. R., Dhomse, S., Falletti, L., Fleming, E., Johnson, B., Jörimann, A., Kovilakam, M., Koren, G., Kuchar, A., Lebas, N., Liang, Q., Liu, C.-C., Mann, G., Manyin, M., Marchand, M., Morgenstern, O., Newman, P., Oman, L. D., Østerstrøm, F. F., Peng, Y., Plummer, D., Quaglia, I., Randel, W., Rémy, S., Sekiya, T., Steenrod, S., Sukhodolov, T., Tilmes, S., Tsigaridis, K., Ueyama, R., Visionsi, D., Wang, X., Watanabe, S., Yamashita, Y., Yu, P., Yu, W., Zhang, J., and Zhuo, Z.: Hunga Tonga–Hunga Ha'apai Volcano Impact Model Observation Comparison (HTHH-MOC) project: experiment protocol and model descriptions, *Geoscientific Model Development*, 18, 5487–5512, <https://doi.org/10.5194/gmd-18-5487-2025>, 2025.
- Zhuo, Z., Wang, X., Zhu, Y., Bednarz, E. M., Fleming, E., Colarco, P. R., Watanabe, S., Plummer, D., Stenchikov, G., Randel, W., Bourassa, A., Aquila, V., Sekiya, T., Schoeberl, M. R., Tilmes, S., Yu, W., Zhang, J., Kushner, P. J., and Pausata, F. S. R.: Comparing Multi-Model Ensemble Simulations with Observations and Decadal Projections of Upper Atmospheric Variations Following the Hunga Eruption, *EGUsphere*, 2025, 1–27, <https://doi.org/10.5194/egusphere-2025-1505>, 2025.